Journal of Computational Physics **157,** 199–233 (2000)
doi:10.1006/jcph.1999.6371, available online at http://www.idealibrary.com on IDEAL®

Numerical Simulations for Radiation Hydrodynamics

II. Transport Limit

W. Wenlong Dai and Paul R. Woodward

School of Physics and Astronomy/Laboratory for Computational Science and Engineering, University of Minnesota, 116 Church Street S.E., Minneapolis, Minnesota 55455

Received July 20, 1998; revised August 31, 1999

A finite difference scheme is proposed for two-dimensional radiation hydrodynamical equations in the transport limit. The scheme is of Godunov-type, in which the set of time-averaged flux needed in the scheme is calculated through Riemann problems solved. In the scheme, flow signals are explicitly treated, while radiation signals are implicitly treated. Flow fields and radiation fields are updated simultaneously. An iterative approach is proposed to solve the set of nonlinear algebraic equations arising from the implicitness of the scheme. The sweeping method used in the scheme significantly reduces the number of iterations or computer CPU time needed. A new approach to further accelerate the convergence is proposed, which further reduces the number of iterations needed by more than one order. No matter how many cells radiation signals propagate in one time step, only an extremely small number of iterations are needed in the scheme, and each iteration costs only about 0.8 percent of computer CPU time which is needed for one time step of a second order accurate and fully explicit scheme. Two-dimensional problems are treated through a dimensionally split technique. Therefore, iterations for solving the set of algebraic equations are carried out only in each one-dimensional sweep. Through numerical examples it is shown that the scheme keeps the principle advantages of Godunov schemes for flow motion. In the time scale of flow motion numerical results are the same as those obtained from a second order accurate and fully explicit scheme. The acceleration of the convergence proposed in this paper may be directly applied to other hyperbolic systems.

Key Words: finite difference; hyperbolic system; hydrodynamics; radiation; transport.

0021-9991/00 $35.00

1. INTRODUCTION

Radiation hydrodynamical equations play an important role in laser fusion [33] and astrophysics [12]. For many years efforts have been underway to develop numerical schemes for radiation hydrodynamical equations, for example, see [15, 16, 21, 32, 36, 37, 42]. In the transport limit, radiation hydrodynamical equations may be written as a hyperbolic system of conservation laws plus emission and absorption of radiation. Physically, there are two kinds of signals involved in the system. One is flow signals including sound waves and entropy waves, and the other is radiation signals. Two distinctive features of the system are that shock waves are involved and radiation signals propagate much more fast than flow signals.

One of the major difficulties of standard numerical methods for the system is to resolve and keep track of shocks involved. To resolve shocks, it is natural to extend established methods for the Euler equations. During the last two decades, numerical methods for capturing shocks have been well developed (for example, see [1, 2, 6–11, 13, 14, 20, 25–27, 29]) among which Godunov schemes are particularly efficient for shock problems. Godunov [1] supposed that initial data could be replaced by a set of piecewise constant data with discontinuities and used the exact solution of Riemann problems to advance piecewise constant data. A major extension of Godunov's scheme was made by van Leer in his MUSCL scheme [6] which used a Riemann solver to advance piecewise linear data. Roe developed an approximate Riemann solver [8] suitable for the use in Godunov schemes. A nonlinear Riemann solver and a contact steepener were developed in the piecewise parabolic method PPM [10, 14]. Key points in Godunov schemes are the use of characteristic formulations, reconstruction of initial data, and an approximate Riemann solver which is suitable for computing a set of time-averaged flux at grid points.

Another difficulty in numerical simulations for radiation hydrodynamics is to treat radiation signals efficiently. If radiation signals are explicitly treated, the size of the time step will be extremely small since the size is restricted by the speed at which radiation signals propagate. For many problems, we are interested in the time scale of flow motion. Therefore, radiation signals may be implicitly treated.

Implicit and implicit–explicit hybrid schemes for the Euler equations have been developed for many years. Beam and Warming [5] proposed an implicit scheme for hyperbolic systems of conservation laws. Engquist and Osher [7] proposed a method for transonic flows. Van Leer and Mulder [17] developed a scheme which is time-accurate for small time steps and turns into a relaxation method for large time steps. Yee *et al.* [18] proposed an implicit TVD scheme for steady states. Glaz and Wardlaw [19] proposed a high-order Godunov scheme for steady supersonic gas dynamics. Fryxell *et al.* [22] developed an implicit–explicit hybrid scheme which extends Godunov schemes to the implicit regime. Jameson and Yoon [23, 24] proposed an implicit scheme which is combined with the multigrid method. Loh and Hui [28] developed a first-order Godunov scheme for steady supersonic flows. Blunt and Rubin [30] extended a TVD scheme to fully implicit and partially implicit regimes. Wilcoxson and Manousiouthakis [31] developed implicit time marching implementation of the essentially non-oscillatory scheme. Dai and Woodward [38, 39] iteratively implemented an implicit–explicit hybrid scheme.

An implicit treatment for time-dependent problems will result in a large set of (nonlinear) algebraic equations at each time step, which, typically, are first linearized and then solved by either a direct method or an iterative method. Direct methods are presented in all traditional

courses of linear algebra. Generally, iterative methods are preferred for implementation on parallel computers. For an iterative method, a significant question is whether an iterative process will actually be successful and will lead to the solution of the algebraic equations. An important aspect in practice is the rate of convergence. A good comparison of five iterative linear solvers for two-dimensional radiation hydrodynamics is recently given in [41]. One of the conclusions from the comparison is that multigrid algorithms are preferred because of heat conduction involved in the diffusion limit. Another problem involved in implicit schemes is the nonlinearity of equations. We don't recommend the classical Newton method for the nonlinearity in implicit schemes, although the Newton method converges fast. Explicit evaluation of Jacobi coefficients in the Newton method is very expensive in implicit schemes.

In this paper, we will develop a numerical scheme for two-dimensional radiation hydrodynamical equations in the transport limit. The scheme is of Godunov-type, in which the set of time-averaged flux needed in the scheme is calculated through Riemann problems solved. The Riemann solver to be developed in this paper is based on characteristic formulations. To resolve shocks, flow signals are explicitly treated in the scheme, while radiation signals are implicitly treated. In this paper, an iterative approach is developed for the set of nonlinear algebraic equations arising from the implicitness of the scheme. Compared to the iterative approach developed in [38, 39], the number of iterations needed is reduced by more than one order. No matter how many cells radiation signals propagate in one time step, only an extremely small number of iterations are needed in the scheme. Toward numerical radiation hydrodynamics, this paper is the continuation of the work reported in [40], in which radiation hydrodynamics is treated in the diffusion limit.

The plan of this paper is as follows. In the second section radiation hydrodynamical equations are given. In the third section we will present a procedure to find characteristic formulations for hyperbolic systems of conservation laws including the set of radiation hydrodynamical equations. A numerical scheme is described in the third section, which includes an explicit treatment for flow signals, an implicit treatment for radiation signals, an iterative approach for a set of nonlinear algebraic equations, an accelerated approach for fast convergence, and treatment for two-dimensional problems. Numerical examples are shown in the fourth section to demonstrate the features of the numerical scheme. The final section is the conclusions of this paper and a brief discussion about future work toward numerical radiation hydrodynamics.

2. BASIC EQUATIONS

Radiating fluid often contains a fraction of radiation momentum and energy. To describe the behavior of such flows we need conservation laws that account for both gas material and radiation contributions to the flow dynamics. In the transport limit, radiation hydrodynamical equations [12] may be written as

$$\frac{\partial \rho}{\partial t} + \nabla \cdot (\rho \mathbf{u}) = 0, \tag{1}$$

$$\frac{\partial}{\partial t}(\rho u_x) + \frac{\partial}{\partial x}(\rho u_x u_x + p) + \frac{\partial}{\partial y}(\rho u_x u_y) = \rho(g_x + \chi f_x), \tag{2}$$

$$\frac{\partial}{\partial t}(\rho u_y) + \frac{\partial}{\partial x}(\rho u_y u_x) + \frac{\partial}{\partial y}(\rho u_y u_y + p) = \rho(g_y + \chi f_y), \tag{3}$$

$$\frac{\partial}{\partial t}\left(\rho u_x + \frac{1}{c} f_x\right) + \frac{\partial}{\partial x}\left(\rho u_x u_x + p + p_r + \frac{1}{c} u_x f_x\right) + \frac{\partial}{\partial y}\left(\rho u_x u_y + \frac{1}{c} u_y f_x\right) = \rho g_x - \frac{1}{c} f_x \frac{\partial u_x}{\partial x}, \tag{4}$$

$$\frac{\partial}{\partial t}\left(\rho u_y + \frac{1}{c} f_y\right) + \frac{\partial}{\partial x}\left(\rho u_y u_x + \frac{1}{c} u_x f_y\right) + \frac{\partial}{\partial y}\left(\rho u_y u_y + p + p_r + \frac{1}{c} u_y f_y\right) = \rho g_y - \frac{1}{c} f_y \frac{\partial u_y}{\partial y}, \tag{5}$$

$$\frac{\partial e_r}{\partial t} + \nabla \cdot [\mathbf{u}(e_r + p_r) + c\mathbf{f}] = \mathbf{u} \cdot \nabla p_r - c\rho\left(\kappa_e e_r - a_r \kappa_p T^4\right), \tag{6}$$

$$\frac{\partial E}{\partial t} + \nabla \cdot [\mathbf{u}(E + p + p_r) + c\mathbf{f}] = \mathbf{u} \cdot \nabla p_r + \chi\rho\mathbf{u} \cdot \mathbf{f}. \tag{7}$$

Here, ρ, p, $\mathbf{u}$, ϵ, and T are the mass density, gas pressure, flow velocity, specific internal energy, and temperature of flow, e_r, $\mathbf{f}$, and p_r are the radiation energy density, radiation flux, and radiation pressure, E is the total energy density,

$$E \equiv \rho\left(\epsilon + \frac{1}{2}\mathbf{u}^2 - \mathbf{g} \cdot \mathbf{r}\right) + e_r,$$

$\mathbf{g}$ and a_r are the gravitational constant and radiation constant, and χ, κ_e, and κ_p are the radiation flux coefficient, radiation energy absorption coefficient, and radiation energy emissivity. The set of Eqs. (1)–(7) is complete if two equations of state are given, one for flow fields, and the other for radiation fields. For the purpose of our test problems, we assume the γ-law for flow fields, $p = (\gamma - 1)\rho\epsilon$, and the Eddington factor for radiation fields,

$$p_r = f_E e_r.$$

Here γ is the ratio of specific heats, and f_E is an Eddington factor.

The term $\mathbf{u} \cdot \nabla p_r$ at the right-hand side of Eqs. (6), (7) is the rate of work done by the fluid against the radiation pressure gradient. The term $\mathbf{f} \cdot \nabla\mathbf{u}/c$ at the right-hand side of Eqs. (4), (5) arises because the radiation energy flux has inertia [12]. In some applications, these two terms, $\mathbf{u} \cdot \nabla p_r$ and $\mathbf{f} \cdot \nabla\mathbf{u}/c$, may be omitted.

General equations for radiation hydrodynamics are far more complicated than those given in Eqs. (1)–(7) which are often called equations in the transport limit. In the transport limit, interaction between radiation fields and gas material is approximately described by a few transport coefficients. These transport coefficients describe the response of gas material to radiation, and, in general, they are frequency dependent or they should be collected for all the radiation frequencies involved. The frequency dependent opacity $\chi(\nu)$ of gas material is contributed from absorption $\chi^a(\nu)$ and scattering $\chi^s(\nu)$. The radiation flux coefficient is related to the opacity through the flux mean

$$\chi = \int [\chi^a(\nu) + \chi^s(\nu)] \frac{f(\nu)}{f}\, d\nu.$$

Here f is the magnitude of radiation flux $\mathbf{f}$ and $f(\nu)$ is monochromatic radiation flux. The energy absorption coefficient κ_e is introduced through absorption mean

$$\kappa_e = \int \chi^a(\nu) \frac{e_r(\nu)}{e_r} \, d\nu.$$

Here $e_r(\nu)$ is the monochromatic radiation energy density. For grey material, the radiation energy emissivity κ_p is introduced through Planck mean

$$\kappa_p = \int \chi^a \frac{B(\nu, T)}{\sigma_R T^4/\pi} \, d\nu.$$

Here $B(\nu, T)$ is the Planck function, and σ_R is the Stefan–Boltzmann constant. Thus, the radiation coefficients are generally solution dependent. In astrophysics, self-gravitation is often important, and therefore, the gravitation coefficient $\mathbf{g}$ is also solution dependent. It is interesting to point out that equations for radiation transfer were analytically studied by Castor [4] a long time ago, and it was found that the form of emission as described in Eq. (6) is true only under the assumption of local thermodynamic equilibrium (LTE) between the radiation field and the gas material. In this paper, we do not intend to deal with radiation hydrodynamics and radiation coefficients in the general case. Instead, for the simplicity, we treat these coefficients, including the gravitation coefficient, as constants, since the set of Eqs. (1)–(7), or a similar set of equations, is widely used in applications. We hope that the approach to be presented here may be useful for more general situations.

For two-dimensional problems, we will employ a dimensionally split technique. Therefore, we write the one-dimensional projection of the above equations, which will be solved in one-dimensional sweeps,

$$\frac{\partial \mathbf{U}}{\partial t} + \frac{\partial \mathbf{F}}{\partial x} = \mathbf{S}. \tag{8}$$

Here

$$\mathbf{U} \equiv \begin{pmatrix} \rho \\ \rho u_x \\ \rho u_y \\ \rho u_x + f_x/c \\ \rho u_y + f_y/c \\ e_r \\ E \end{pmatrix}, \qquad \mathbf{F}(\mathbf{U}) \equiv \begin{pmatrix} \rho u_x \\ \rho u_x^2 + p \\ \rho u_x u_y \\ F_m \\ \rho u_x u_y + u_x f_y/c \\ u_x e_r + c f_x \\ u_x(E + p) + c f_x \end{pmatrix},$$

$$\mathbf{S}(\mathbf{U}) \equiv \begin{pmatrix} 0 \\ \rho(g_x + \chi f_x) \\ 0 \\ \rho g_x - \frac{\partial u_x}{\partial x} f_x/c \\ 0 \\ -p_r \frac{\partial u_x}{\partial x} - \rho\left(\kappa_e e_r - a_r \kappa_p T^4\right) \\ -p_r \frac{\partial u_x}{\partial x} + \chi \rho u_x f_x \end{pmatrix},$$

and F_m is the flux for total momentum,

$$F_m \equiv \rho u_x^2 + p + p_r + \frac{1}{c} u_x f_x.$$

3. CHARACTERISTIC FORMULATIONS

In this section, we will discuss characteristic formulations for radiation hydrodynamical equations. The procedure to be presented here may be applied to general hyperbolic systems of conservation laws described by Eq. (8) with n unknowns, $\mathbf{U} = (u_1, u_2, \ldots, u_n)^T$ and $\mathbf{F} = (f_1, f_2, \ldots, f_n)^T$.

We write Eq. (8) in the form

$$\frac{\partial \mathbf{U}}{\partial t} + \mathbf{A}\frac{\partial \mathbf{U}}{\partial x} = \mathbf{S}. \tag{9}$$

Here, $\mathbf{A}(\mathbf{U})$ is a $n \times n$ matrix $\{a_{ij}\}$, $a_{ij} \equiv \partial f_i / \partial u_j$, and u_j and f_i are the jth and ith element of $\mathbf{F}$ and $\mathbf{U}$. In the following, c_k and $\mathbf{L}_k$ $[\equiv (l_1, l_2, \ldots, l_n)]$ denote the kth eigenvalue of the matrix $\mathbf{A}(\mathbf{U})$ and the associated left eigenvector, i.e.,

$$\mathbf{L}_k \mathbf{A}(\mathbf{U}) = c_k \mathbf{L}_k, \qquad k = 1, 2, \ldots, n. \tag{10}$$

Obviously, c_k and $\mathbf{L}_k$ both are functions of $\mathbf{U}$. Actually, c_k, called a characteristic speed, is a wave speed of the system. Multiplying Eq. (9) from the left by the eigenvector $\mathbf{L}_k$, and using Eq. (10) we have

$$\mathbf{L}_k \left(\frac{\partial \mathbf{U}}{\partial t} + c_k \frac{\partial \mathbf{U}}{\partial x} \right) = \mathbf{L}_k \mathbf{S}. \tag{11}$$

The equation $dx/dt = c_k(\mathbf{U})$ defines a curve in $x - t$ space, which is called a characteristic curve. Along the characteristic curve, we have

$$d\mathbf{U} = \left(\frac{\partial \mathbf{U}}{\partial t} + c_k \frac{\partial \mathbf{U}}{\partial x} \right) dt. \tag{12}$$

Using Eq. (11), along the characteristic curve $dx/dt = c_k$ we have

$$L_k(\mathbf{U})(d\mathbf{U} - \mathbf{S}dt) = 0.$$

If dR_k is used to denote

$$dR_k \equiv L_k(\mathbf{U})(d\mathbf{U} - \mathbf{S}dt), \tag{13}$$

then along the characteristic curve, dR_k, which is normally called a differential of Riemann invariant, remains vanishing:

$$dR_k = 0. \tag{14}$$

Following this procedure, for the system described by Eq. (8) we may find five characteristic speeds, u_x, $u_x \pm c_s$, and $\pm c_r$. Here c_s is the sound speed $c_s \equiv \sqrt{\gamma p/\rho}$ and c_r is the radiation speed $c_r \equiv c\sqrt{f_E}$. The differentials of Riemann invariant for the characteristic speed u_x are

$$dR_0 = (dp - \Delta p) - c_s^2 d\rho, \tag{15}$$

$$du_y = 0, \tag{16}$$

$$df_y = 0. \tag{17}$$

Here

$$\Delta p \equiv c\rho\left(\kappa_e e_r - \kappa_p a_r T^4\right)dt \Big/ \left(\frac{\partial \epsilon}{\partial p}\right)_\rho.$$

Two differentials of Riemann invariants for two sound waves are

$$dR_{s\pm} = (dp - \Delta p) \pm \rho c_s (du_x - \Delta u_x). \tag{18}$$

Here

$$\Delta u_x \equiv (g_x + \chi f_x)dt.$$

These differentials of Riemann invariants are the same as those for the Euler equations except for the effect of the source term **S**. Two differentials of Riemann invariants for two radiation signals are

$$\begin{aligned} dR_{r\pm} = {} & \rho\left(c_r^2 - c_s^2\right)[c(df_x - \Delta f_x) \pm c_r(de_r - \Delta e_r)] \\ & + [2cf_x \pm (e_r + p_r)c_r][(dp - \Delta p) \pm \rho c_r (du_x - \Delta u_x)]. \end{aligned} \tag{19}$$

Here

$$\Delta e_r \equiv -c\rho\left(\kappa_e e_r - \kappa_p a_r T^4\right)dt,$$

$$\Delta f_x \equiv -c\chi\rho f_x dt.$$

4. NUMERICAL SCHEMES

Considering a grid $\{x_i\}$, integrating Eq. (8) in a grid cell $x_i \le x \le x_{i+1}$ and over a time step $0 \le t \le \Delta t$, we have

$$\mathbf{U}_i^n = \mathbf{U}_i + \frac{\Delta t}{\Delta x_i}[\mathbf{F}(\bar{\mathbf{U}}_i) - \mathbf{F}(\bar{\mathbf{U}}_{i+1})] + \mathbf{S}_i^h \Delta t. \tag{20}$$

Here Δx_i is the width of the cell, Δt is the time step, $\mathbf{U}_i$ and $\mathbf{U}_i^n$ are two cell-averaged values of **U** at the initial time and at the new time $t = \Delta t$, $\bar{\mathbf{U}}_i$ is a time-averaged value of **U** over the time step at the grid point $x = x_i$, and they are defined as, for example,

$$\mathbf{U}_i^n \equiv \frac{1}{\Delta x_i}\int_{x_i}^{x_{i+1}} \mathbf{U}(\Delta t, x)\, dx, \qquad \bar{\mathbf{U}}_i \equiv \frac{1}{\Delta t}\int_0^{\Delta t} \mathbf{U}(t, x_i)\, dt. \tag{21}$$

$\mathbf{S}_i^h$ in Eq. (20) is the source term $\mathbf{S}(\mathbf{U})$ evaluated at $\mathbf{U}_i^h[\equiv \frac{1}{2}(\mathbf{U}_i + \mathbf{U}_i^n)]$. To get Eq. (20), we have approximately used the product of cell (or time) averaged values as the cell (or time) averaged value of a product. Therefore, one of the key points in the scheme is to approximately calculate the time-averaged values $\bar{\mathbf{U}}_i$ and the evaluation of $\mathbf{S}_i^h$, which will be discussed in the following five subsections.

The time-averaged values $\bar{\mathbf{U}}_i$ needed in Eq. (20) are calculated through Riemann problems approximately solved. A Riemann problem is an initial value problem, Eq. (8), with the initial condition

$$\mathbf{U}(0, x) = \begin{cases} \mathbf{U}_L & \text{if } x < 0 \\ \mathbf{U}_R & \text{if } x > 0. \end{cases} \tag{22}$$

Here $\mathbf{U}_L$ and $\mathbf{U}_R$ are a pair of left and right states.

4.1. *Explicit Treatment for Flow Signals*

In order to resolve shocks, we treat flow signals explicitly. We restrict the size of time step so that sound waves propagate no more than one grid cell. For a given pair of left and right states, we approximately calculate the time-averaged values of u_x and p at a grid point, $\bar{u}_i$ and $\bar{p}_i$, through solving the following set of two equations

$$\bar{p}_i - (p_L + \Delta p_L) + \rho_L c_{sL}[\bar{u}_{xi} - (u_L + \Delta u_{xL})] = 0, \tag{23}$$

$$\bar{p}_i - (p_R + \Delta p_R) + \rho_R c_{sR}[\bar{u}_{xi} - (u_R + \Delta u_{xR})] = 0. \tag{24}$$

Here the subscript L (or R) denotes the evaluation at the left (or right) state. Equations (23), (24) come from the property of Riemann invariants for two sound waves that along the characteristic curves $dx/dt = u_x \pm c_s$, $dR_{s\pm} = 0$. To keep the difference Eq. (20) second order accurate in time, we need the set of time-averaged flux accurate to $O(\Delta t)$. Since Δu_x and Δp, as in their definition, are already proportional to Δt, we may evaluate Δu_x and Δp at the initial time for the use in Eqs. (23), (24). Therefore, we may explicitly find the time-averaged values $\bar{p}_i$ and $\bar{u}_{xi}$ and keep the difference Eq. (20) second order accurate in time.

Now we would like to discuss the evaluation of left and right states used in Eqs. (23), (24). If we were working on a Lagrangian algorithm, the left (or right) state used in Eqs. (23), (24) should be the state of the left (or right) cell to the grid point in the lowest order and should be the averaged value on a domain of dependence in a higher order. But, since we are working on an Eulerian algorithm, the left (or right) state to be used in Eqs. (23), (24) is not necessarily the state in the left (or right) cell to the grid point.

Considering the Riemann problem arising at the grid point $x = x_i$, as an example, we describe the calculation for the effective u_{xL} and p_L used in Eqs. (23), (24). If $(u_{xi-1} + c_{si-1}) \geq 0$ and $(u_{xi} + c_{si}) \geq 0$, then we consider the domain-average on the domain $x_i - (u_{xi-1} + c_{si-1})\Delta t < x \leq x_i$ the effective left state. If $(u_{xi-1} + c_{si-1}) < 0$ and $(u_{xi} + c_{si}) < 0$, then we consider the domain-average on the domain $x_i < x < x_i - (u_{xi} + c_{si})\Delta t$ the effective left state. If $(u_{xi-1} + c_{si-1}) \geq 0$ and $(u_{xi} + c_{si}) < 0$, then we consider the domain-average on the domain $x_i - (u_{xi-1} + c_{si-1})\Delta t < x < x_i - (u_{xi} + c_{si})\Delta t$ the effective left state. If $(u_{xi-1} + c_{si-1}) < 0$ and $(u_{xi} + c_{si}) \geq 0$, we are in the middle of a rarefaction fan. In this case, we consider the average of two states in the $(i-1)$st and ith cells with weighting factors

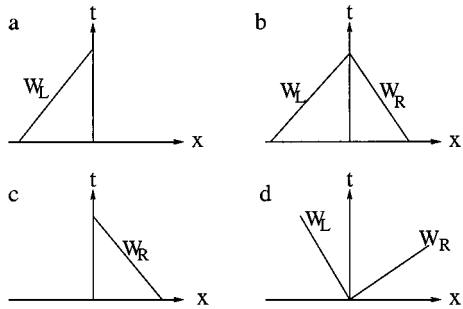

FIG. 1. An illustration for effective left and right states. (a) If $(u_{xL}+c_{sL})\geq 0$ and $(u_{xR}+c_{sR})\geq 0$, then the domain-average on the domain $x_i-(u_{xL}+c_{sL})\Delta t<x\leq x_i$ is the effective left state. (b) If $(u_{xL}+c_{sL})\geq 0$ and $(u_{xR}+c_{sR})<0$, then the domain-average on the domain $x_i-(u_{xL}+c_{sL})\Delta t<x<x_i-(u_{xR}+c_{sR})\Delta t$ is the effective left state. (c) If $(u_{xL}+c_{sL})<0$ and $(u_{xR}+c_{sR})<0$, then the domain-average on the domain $x_i<x<x_i-(u_{xR}+c_{sR})\Delta t$ is the effective left state. (d) If $(u_{xL}+c_{sL})<0$ and $(u_{xR}+c_{sR})\geq 0$, the average of the left and right cell-averages with weighting factors $(u_{xR}+c_{sR})$ and $-(u_{xL}+c_{sL})$ is the left state.

$(u_{xi}+c_{si})$ and $-(u_{xi-1}+c_{si-1})$ the effective left state. This calculation is illustrated in Fig. 1. The effective right state may be similarly calculated based on the signs of (u_x-c_s) on the two adjacent cells.

From Eqs. (15)–(17), we may also explicitly find the time-averaged values of ρ, u_y, and f_y at the grid point, $\bar{\rho}_i$, $\bar{u}_{yi}$, and $\bar{f}_{yi}$, through the three equations

$$\bar{p}_i-\left(p_i^0+\Delta p\right)-c_s^2\left(\bar{\rho}_i-\rho_i^0\right)=0, \tag{25}$$

$$\bar{u}_y=u_{yi}^0, \tag{26}$$

$$\bar{f}_y=f_{yi}^0. \tag{27}$$

Here, the superscript 0 denotes the domain-average over the domain between x_i and $(x_i+\bar{u}_{xi}\Delta t)$. As Δp and Δu_x used in Eqs. (23), (24), we explicitly evaluate Δp used in Eq. (25).

For the calculation of domain-averages, for example, of gas pressure p, interpolations are needed to determine the structure of p inside each grid cell. Although more sophisticated interpolations may be used, we use a linear interpolation in this paper for the cell structure. Therefore, the values of p at the grid points $x=x_i$ and $x=x_{i+1}$, p_{il} and p_{ir}, are $p_i-k_i\Delta x_i/2$ and $p_i+k_i\Delta x_i/2$. Here the slope k_i is determined by $(p_{i+1}-p_{i-1})/(\Delta x_{i-1}/2+\Delta x_i+\Delta x_{i+1}/2)$. After we obtain the values at grid points, the monotonicity constraint originally suggested by van Leer [6] is applied to these values at grid points, i.e., no values interpolated within a cell shall lie outside the range defined by the cell-average for this cell and its two neighbors. Therefore, after the monotonicity applied, the cell structure will be

$$p_i(x)=p_i+K_i[x-(x_i+\Delta x_i/2)]/\Delta x_i,$$

and

$$K_i=s*\min[2*\max(s*\Delta p_i,0),2*\max(s*\Delta p_{i-1},0),s*(p_{ir}-p_{il})].$$

Here

$$s\equiv\operatorname{sign}(p_{ir}-p_{il}),\qquad \Delta p_i\equiv p_{i+1}-p_i.$$

Through this explicit treatment for flow signals, we may obtain the time-averaged values $\bar{\rho}_i$, $\bar{p}_i$, $\bar{u}_{xi}$, $\bar{u}_{yi}$, and $\bar{f}_{yi}$. Using these time-averaged values, we explicitly update ρ_i, u_{yi} and f_{yi} to get ρ_i^n, u_{yi}^n, and f_{yi}^n.

4.2. *Implicit Treatment for Radiative Signals*

In this subsection, we will discuss the implicit calculation of the time-averaged values of f_x and e_r at grid points, which are needed in Eq. (20). For the convenience of our discussion, we write Eq. (20) here again

$$\rho_i^n u_{xi}^n - \rho_i u_{xi} + \frac{\Delta t}{\Delta x_i}\left[\bar{\rho}_{i+1}\bar{u}_{xi+1}^2 + \bar{p}_{i+1} - \bar{\rho}_i u_{xi}^2 - \bar{p}_i\right] - \rho_i^n\left(g_x + \chi f_{xi}^n\right)\Delta t = 0, \tag{28}$$

$$\rho_i^n u_{xi}^n - \rho_i u_{xi} + \frac{1}{c}\delta f_{xi}^n + \frac{\Delta t}{\Delta x_i}(\bar{F}_{mi+1} - \bar{F}_{mi}) + \frac{\Delta t}{c\Delta x_i}(\bar{u}_{xi+1} - \bar{u}_{xi})\, f_{xi}^n - \Delta t g_x \rho_i^n = 0, \tag{29}$$

$$\delta e_{ri}^n + \frac{\Delta t}{\Delta x_i}[\bar{u}_{xi+1}\bar{e}_{ri+1} + c\,\bar{f}_{xi+1} - \bar{u}_{xi}\bar{e}_{ri} - c\,\bar{f}_{xi}] + p_{ri}^n\frac{\Delta t}{\Delta x_i}(\bar{u}_{xi+1} - \bar{u}_{xi}) - \Delta t c\rho_i^n\left[\kappa_e e_{ri}^n - \kappa_p a_r\left(T_i^n\right)^4\right] = 0, \tag{30}$$

$$\delta E_i^n + \frac{\Delta t}{\Delta x_i}[\bar{u}_{xi}(\bar{E}_i + \bar{p}_i) + c\,\bar{f}_{xi}] + \frac{\Delta t}{\Delta x_i}p_{ri}^n(\bar{u}_{xi+1} - \bar{u}_{xi}) - \chi\,\Delta t\rho_i^n u_{xi}^n f_{xi}^n = 0. \tag{31}$$

Here $\delta e_{ri}^n \equiv e_{ri}^n - e_{ri}$, and $\delta E_i^n \equiv E_i^n - E_i$. In Eqs. (28)–(31), we have evaluated the source terms at $t = \Delta t$, which will make Eqs. (28)–(31) only first order accurate in time. As we will show in this subsection, we use Eqs. (28)–(31) only for two sets of values. One is the set of time-averaged flux, which is needed in Eq. (20) and has to be only first order accurate to keep Eq. (20) second order accurate in time. The other set of values is the first order accurate $\mathbf{U}_i^n$, which will be used in the evaluation of the source term $\mathbf{S}_i^h$ in Eq. (20)

$$\mathbf{S}_i^h = \mathbf{S}\left[\frac{1}{2}\left(\mathbf{U}_i + \mathbf{U}_i^n\right)\right].$$

Although these two sets of values are first order accurate, after we plug these two sets of values into Eq. (20) the updated values $\mathbf{U}_i^n$ are second order accurate. Thus the numerical scheme being described in this paper actually has two steps, predictor and corrector. In the predictor step, we find first order accurate (in time) flux and cell-averages $\mathbf{U}_i^n$. In the corrector step we put the first order accurate solution, $\mathbf{F}(\bar{\mathbf{U}}_i)$ and $\mathbf{U}_i^n$, back into Eq. (20) to update $\mathbf{U}_i$.

In the time scale of flow motion, a time step Δt is so large that $c_r\,\Delta t/\Delta x_i$ is much larger than unity. Therefore, we use the backward Euler formulation for $\bar{e}_{ri}$ and $\bar{f}_{xi}$,

$$\bar{e}_{ri} \approx e_{ri}^{ln}, \qquad \bar{f}_{xi} \approx f_{xi}^{ln}. \tag{32}$$

Here $e_{ri}^{ln} \equiv e_r(\Delta t, x_i)$, $f_{xi}^{ln} \equiv f_x(\Delta t, x_i)$, and the superscript *ln* stands for "*l*eft edge at the *n*ew time."

As shown in Fig. 2, the values of f_{xi}^{ln} and e_{ri}^{ln} may be approximately calculated through tracing two radiation characteristic curves, which pass through the point $(x_i, \Delta t)$, back to

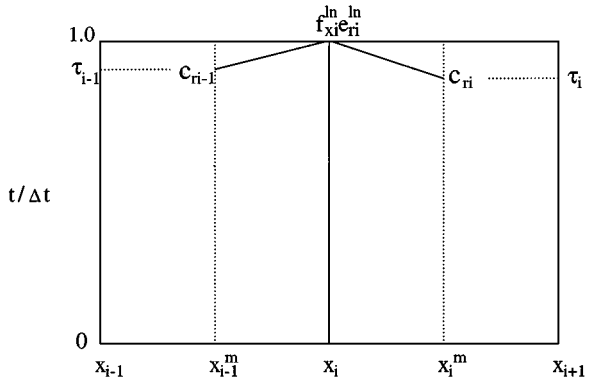

FIG. 2. The values of e_{ri}^{ln} and f_{xi}^{ln} are calculated through tracing two characteristic curves back to the centers of two neighboring cells.

the centers of two neighboring cells. From Eq. (19) we have

$$\begin{aligned} & a_{i-1}\{c[f_{xi}^{ln} - f_x(\tau_{i-1}\Delta t, x_{i-1}^m) - \Delta f_{xi-1}] + c_r[e_{ri}^{ln} - e_r(\tau_{i-1}\Delta t, x_{i-1}^m) - \Delta e_{ri-1}]\} \\ & \quad + b_{i-1}^{+}\{\bar{p}_i - p(\tau_{i-1}\Delta t, x_{i-1}^m) - \Delta p_{i-1} \\ & \quad + c_r\rho_{i-1}[\bar{u}_{xi} - u_x(\tau_{i-1}\Delta t, x_{i-1}^m) - \Delta u_{xi-1}]\} = 0, \end{aligned} \tag{33}$$

$$\begin{aligned} & a_i\{c[f_{xi}^{ln} - f_x(\tau_i\Delta t, x_i^m) - \Delta f_{xi}] - c_r[e_{ri}^{ln} - e_r(\tau_i\Delta t, x_i^m) - \Delta e_{ri}]\} \\ & \quad + b_i^{-}\{\bar{p}_i - p(\tau_i\Delta t, x_i^m) - \Delta p_i + c_r\rho_i[\bar{u}_{xi} - u_x(\tau_i\Delta t, x_i^m) - \Delta u_{xi}]\} = 0. \end{aligned} \tag{34}$$

Here, x_i^m is the center of a cell and $\tau_i\Delta t$ is the time at the intersection between the line $x = x_i^m$ and the characteristic curve passing through the point $(x_i, \Delta t)$, a and b are the coefficients of differentials of Riemann invariants Eq. (19), and they are

$$a \equiv \rho(c_r^2 - c_s^2), \qquad b^{\pm} \equiv 2cf_x \pm c_r(e_r + p_r).$$

It is easy to find that

$$\tau_i = 1 - \frac{\Delta x_i}{2c_r\Delta t}.$$

As stated before, to keep e_{ri}^{ln} and f_{xi}^{ln} first order accurate, Δp_i, Δu_{xi}, Δe_{ri}, and Δf_{xi} in Eqs. (33), (34) may be explicitly evaluated at the initial time. The value of a variable, for example, f_x, at $(\tau_i\Delta t, x_i^m)$ in Eqs. (33), (34) is approximately calculated from cell-averages f_{xi} and f_{xi}^n through a linear interpolation in time,

$$f_x(\tau_i\Delta t, x_i^m) = f_{xi} + \tau_i\delta f_{xi}^n.$$

Solving Eqs. (33), (34) for e_{ri}^{ln} and f_{xi}^{ln}, we may write e_{ri}^{ln} and f_{xi}^{ln} in terms of $\mathbf{U}_i^n$:

$$\begin{aligned} e_{ri}^{ln} = e_{ri}^0 & + \frac{1}{2}\tau_i\left[\delta e_{ri}^n - \frac{c}{c_r}\delta f_{xi}^n - \frac{1}{c_r}\eta_i\delta p_i^n + \rho_i\eta_i\delta u_{xi}^n\right] \\ & + \frac{1}{2}\tau_{i-1}\left[\delta e_{ri-1}^n + \frac{c}{c_r}\delta f_{xi-1}^n + \frac{1}{c_r}\zeta_{i-1}\delta p_{i-1}^n + \rho_{i-1}\zeta_{i-1}\delta u_{xi-1}^n\right], \end{aligned} \tag{35}$$

$$f_{xi}^{ln} = f_{xi}^{0} + \frac{1}{2c}\tau_i\left[c\delta f_{xi}^{n} - c_r\delta e_{ri}^{n} + \eta_i\delta p_i^{n} - c_r\eta_i\rho_i\delta u_{xi}^{n}\right] + \frac{1}{2c}\tau_{i-1}\left[c\delta f_{xi-1}^{n} + c_r\delta e_{ri-1}^{n} + \zeta_{i-1}\delta p_{i-1}^{n} + c_r\zeta_{i-1}\rho_{i-1}\delta u_{xi-1}^{n}\right]. \quad (36)$$

Here

$$e_{ri}^{0} \equiv \frac{1}{2}(e_{ri} + \Delta e_{ri} + e_{ri-1} + \Delta e_{ri-1}) - \frac{c}{2c_r}(f_{xi} + \Delta f_{xi} - f_{xi-1} - \Delta f_{xi-1}) + \frac{1}{2c_r}\eta_i[\bar{p}_i - p_i - \Delta p_i - c_r\rho_i(\bar{u}_{xi} - u_{xi} - \Delta u_{xi})] - \frac{1}{2c_r}\zeta_{i-1}[\bar{p}_i - p_{i-1} - \Delta p_{i-1} + c_r\rho_{i-1}(\bar{u}_{xi} - u_{xi-1} - \Delta u_{xi-1})], \quad (37)$$

$$f_{xi}^{0} \equiv \frac{1}{2}\left[f_{xi} + \Delta f_{xi} + f_{xi-1} + \Delta f_{xi-1} - \frac{c_r}{c}(e_{ri} + \Delta e_{ri} - e_{ri-1} - \Delta e_{ri-1})\right] - \frac{1}{2c}\eta_i[\bar{p}_i - p_i - \Delta p_i - c_r\rho_i(\bar{u}_{xi} - u_{xi} - \Delta u_{xi})] - \frac{1}{2c}\zeta_{i-1}[\bar{p}_i - p_{i-1} - \Delta p_{i-1} + c_r\rho_{i-1}(\bar{u}_{xi} - u_{xi-1} - \Delta u_{xi-1})]. \quad (38)$$

$$\eta \equiv \frac{2cf_x - c_r(e_r + p_r)}{\rho\left(c_r^2 - c_s^2\right)}, \qquad \zeta \equiv \frac{2cf_x + c_r(e_r + p_r)}{\rho\left(c_r^2 - c_s^2\right)}.$$

The coefficients in Eqs. (35)–(38) depend on ρ, p, e_r, and f_x. To keep e_{ri}^{ln} and f_{xi}^{ln} first order accurate, we may evaluate the coefficients at either $t = 0$ or $t = \Delta t$. In our code, for the coefficients we use the initial values of ρ and p, and the values at $t = \Delta t$ for e_r and f_x.

If we insert Eqs. (35), (36) into Eqs. (28)–(31), we will get a set of nonlinear algebraic equations for a set of cell-averaged values, p_i^n, u_{xi}^n, e_{ri}^n, and f_{xi}^n. Since we have used the backward Euler formulation for radiation signals, the numerical errors in radiation signals undergo a quick damping in the time scale of flow motion.

4.3. *Iterative Approach*

Equations (28)–(31), (35), (36) may be iteratively solved. We insert Eqs. (35), (36) into Eqs. (28)–(31) and get a set of nonlinear algebraic equations for cell-averages p_i^n, u_{xi}^n, e_{ri}^n, and f_{xi}^n. To treat the nonlinearity of the resulting equations, we write the product of two unknowns, for example, u_{xi}^n and f_{xi}^n, as

$$u_{xi}^{n} f_{xi}^{n} = u_{xi}^{n}\delta f_{xi}^{n} + f_{xi}\delta u_{xi}^{n} + u_{xi} f_{xi}.$$

Similarly,

$$\left(T_i^n\right)^4 = \left[\left(T_i^n + T_i\right)\delta T_i^n + T_i^2\right]^2.$$

After some straightforward manipulations, we may write the set of algebraic equations in the form

$$\mathbf{Q}_i\delta\mathbf{V}_i^n = \mathbf{P}_i\delta\mathbf{V}_{i+1}^n + \mathbf{M}_i\delta\mathbf{V}_{i-1}^n + \mathbf{C}_i. \quad (39)$$

Here $\mathbf{V}_i^n$ is a vector for unknowns,

$$\mathbf{V}_i^n \equiv \begin{pmatrix} p_i^n \\ u_{xi}^n \\ e_{ri}^n \\ f_{xi}^n \end{pmatrix},$$

$\delta\mathbf{V}_i^n \equiv \mathbf{V}_i^n - \mathbf{V}_i$, $\mathbf{Q}_i$, $\mathbf{P}_i$, and $\mathbf{M}_i$ are three matrices which depend on unknowns $\mathbf{V}_i^n$, and $\mathbf{C}_i$ is a vector which is independent of unknowns $\mathbf{V}_i^n$. The set of Eq. (39) is what we want to solve, which is nonlinear. For the nonlinearity we have not introduced any approximation, such as any linearizing procedure, in Eq. (39). Therefore, our treatment for the nonlinearity is completely nonlinear.

The set of Eq. (39) may be iteratively solved, for example, through a red–black approach, or Gauss–Seidel method. In a red–black approach, numerical cells are divided into two sets, $\{i = 2j+1;\ j = 1, 2, \ldots\}$, and $\{i = 2j;\ j = 1, 2, \ldots\}$, which are called red and black sets. For each iteration, we solve Eq. (39) for the red set first with the black set fixed, and then solve Eq. (39) for the black set with the red set fixed. Therefore, information propagates two grid cells for each iteration in both directions in the red–black approach. In the Gauss–Seidel method, $\delta\mathbf{V}_i^n$ is evaluated through most recent values for $\mathbf{V}_{i+1}^n$ and $\mathbf{V}_{i-1}^n$. We would like to mention that for the set of Eq. (39) the convergence of the Gauss–Seidel method is slower than the red-black approach. But, if a sweeping mechanism is added to the Gauss–Seidel method, the resulting sweeping method converges much more fast than the red-black approach. The sweeping mechanism we used in this paper is the following [35]. In the first iteration, we solve Eq. (39) for $i = 1$ first, then for $i = 2$, and so on, until for $i = N$. In the next iteration, Eq. (39) is solved for i from $i = N$ to $i = 1$, as shown in Fig. 3 in which the arrows indicate the orders solving Eq. (39) for different i in each iteration. We would like to mention that the matrices $\mathbf{Q}_i$, $\mathbf{P}_i$, and $\mathbf{M}_i$ in Eq. (39) have to be adapted to the new solution values after each iteration, but they do not have to be adapted to the new solution values until a complete iteration is finished.

To show the convergence, we initially set up a sound wave and a radiation wave,

$$\frac{dR_0}{dx} = 0, \qquad \frac{dR_{s-}}{dx} = 0, \qquad \frac{dR_{r-}}{dx} = 0,$$
$$\frac{dR_{s+}}{dx} = 0.01\sin(2\pi x), \qquad \frac{dR_{r+}}{dx} = 0.01\sin(2\pi x).$$

The initial profiles for physical variables are obtained through solving this set of ordinary differential equations for ρ, p, u_x, e_r, and f_x. The sound speed is about unity and the speed of radiation signals is 10^4. We turn off all the radiation coefficients in this example. When the time step $\Delta t = 5 \times 10^{-5}$ is used, the Courant number for radiation signals $c_r \Delta t/\Delta x$ is about

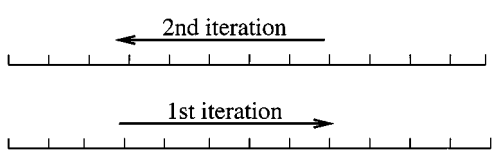

FIG. 3. An illustration for the sweeping method. The arrows indicate the orders to implement Eq. (39) in each cell.

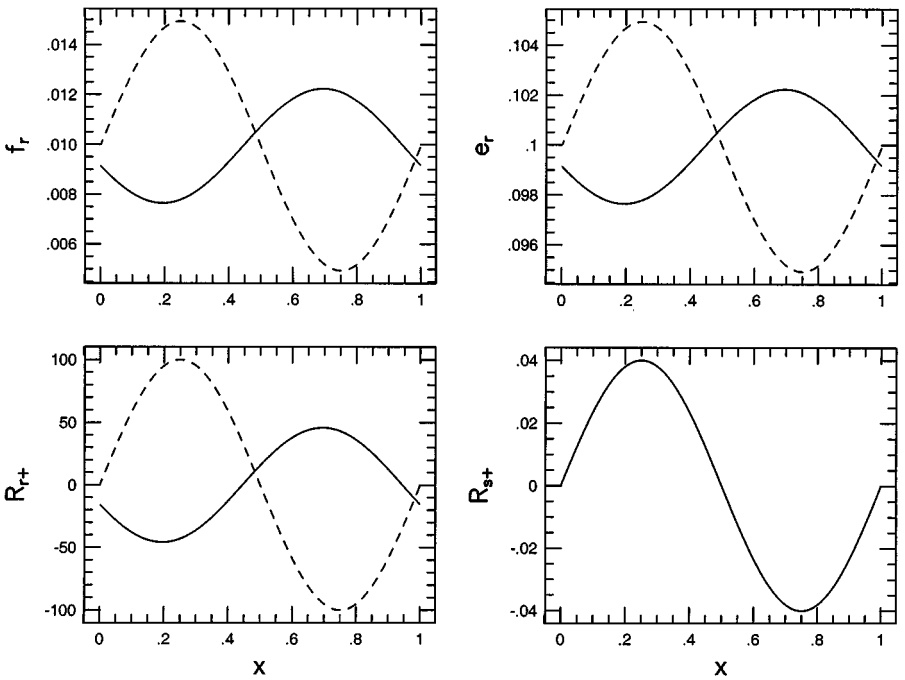

FIG. 4. The initial condition (dashed lines) and the solution after one time step Δt (solid lines). $\Delta t c_r / \Delta x$ is 128.

128. Here $\Delta x = 1/256$. The dashed and solid lines in Fig. 4 show the initial profiles and profiles after one time step, respectively. Figure 5 shows the convergence for the red–black approach and sweeping method. The error Δ in Fig. 5 is the maximum of the discrepancy between the left-hand and right-hand sides of Eqs. (28)–(31) for all grid cells.

As stated before, the scheme presented in this paper is not designed to resolve the time scale of radiation signals. We are interested only in the time scale of flow motion. Therefore,

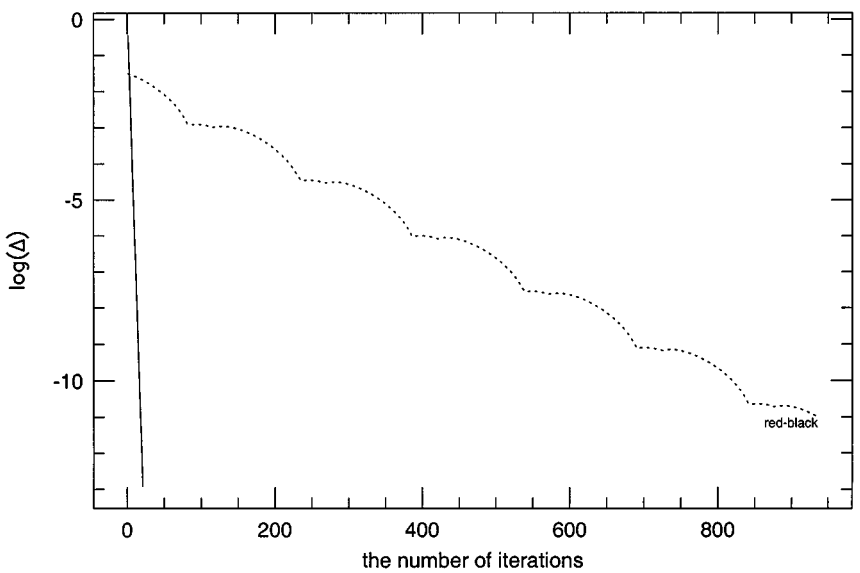

FIG. 5. The convergence obtained from red–black (dashed line) and the sweeping method (solid line) when $\Delta t c_r / \Delta x$ is about 128.

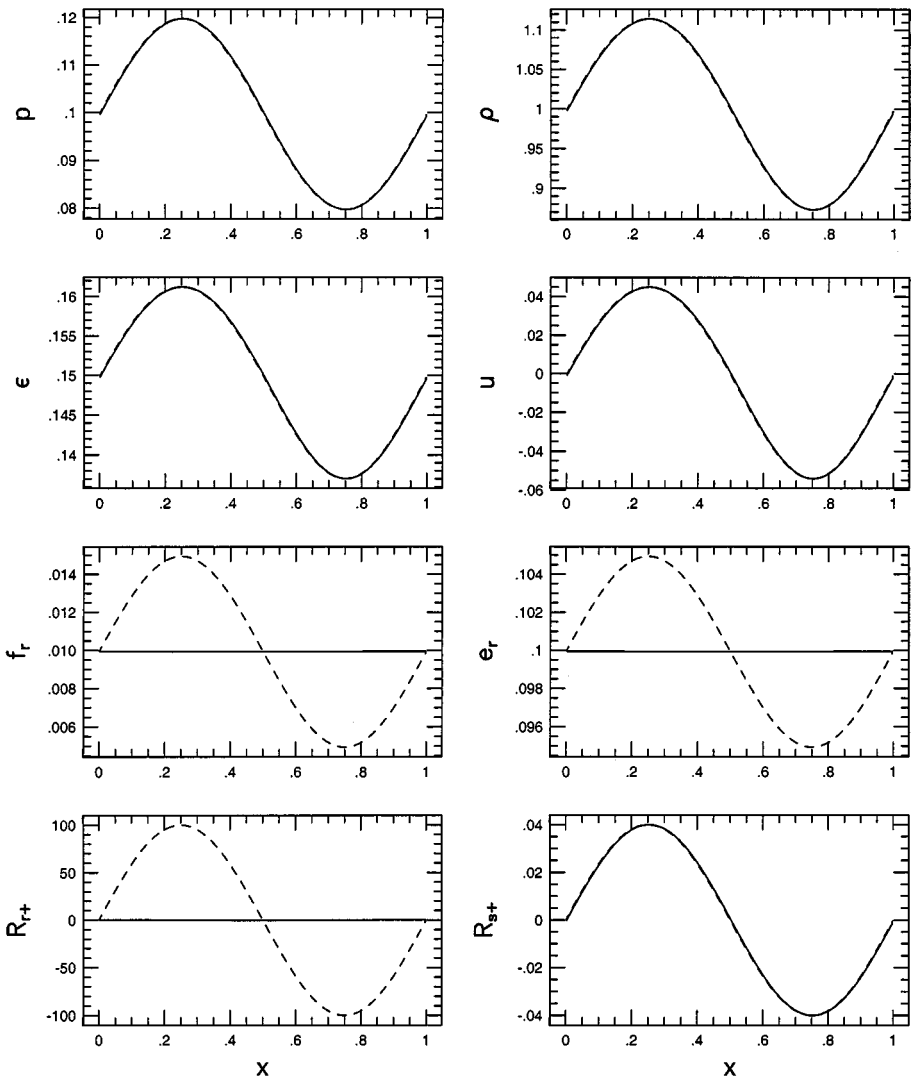

FIG. 6. The initial condition (dashed lines) and the solution after one time step Δt (solid lines). $\Delta t c_r / \Delta x$ is 17,920.

for the problem described above, the size of time step may be much larger. We increase the time step to $\Delta t = 7 \times 10^{-3}$ for the problem above, so that the Courant number for radiation signals is about 1.792×10^4 and the Courant number for the sound wave $c_s \Delta t / \Delta x$ is about 0.84. The solid lines in Fig. 6 show the profiles after one time step, and Fig. 7 shows the convergence of the sweeping method.

4.4. *Acceleration of Convergence*

From numerical experiments, we noticed that the sweeping method converges extremely fast for those problems with known boundary values, $\mathbf{V}_0^n$ and $\mathbf{V}_{N+1}^n$, compared to other problems. Suppose we have a problem in which the initial condition is the same as that just described above, but values at boundaries are fixed. If a grid with $N = 256$ grid points and a time step $\Delta t = 7 \times 10^{-3}$ are used for the problem, we will get the convergence shown in

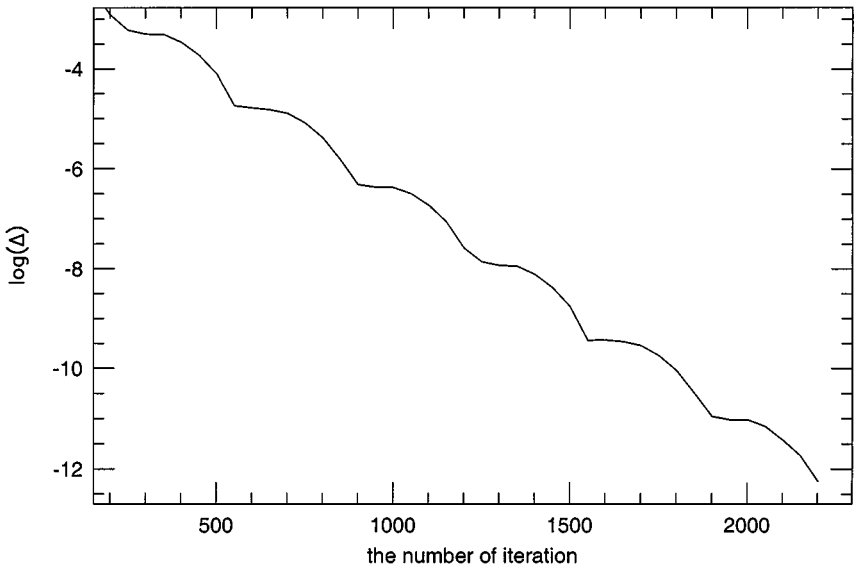

FIG. 7. The convergence obtained from the sweeping method when $\Delta t c_r / \Delta x$ is about 17,920.

Fig. 8, in which the dashed line is obtained from the red–black approach and the solid line is obtained from the sweeping method.

From the phenomena shown in Fig. 8, we have developed an iterative approach for general boundary conditions, which converges much more fast than the sweeping method. Suppose we have a problem with boundary conditions written in general forms

$$H_j\left(\mathbf{V}_0^n, \mathbf{V}_{N+1}^n, \mathbf{V}_1^n, \mathbf{V}_N^n\right) = 0, \qquad j = 1, 2, \ldots, 8. \tag{40}$$

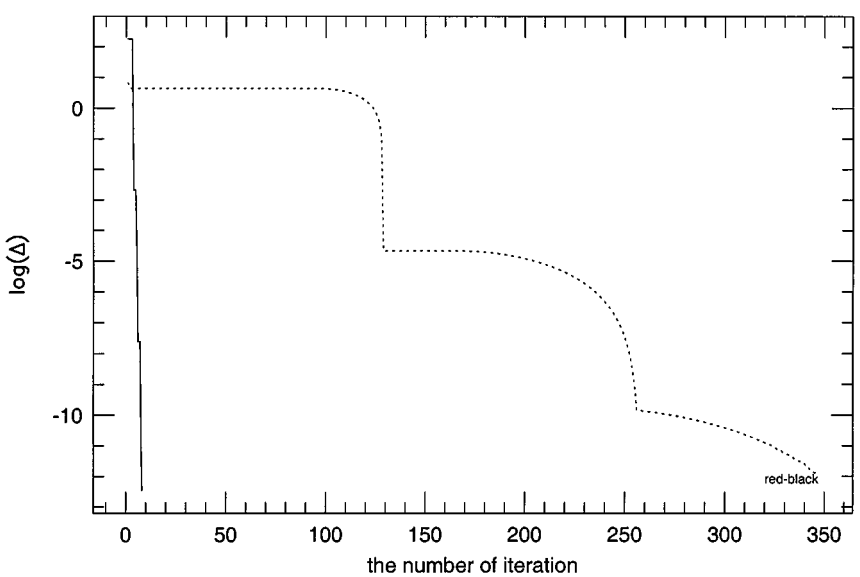

FIG. 8. The convergence obtained from the red–black approach (dashed line) and the sweeping method (solid line) for a problem with values at two fake cells are fixed when $\Delta t c_r / \Delta x$ is 17,920.

Here $\mathbf{V}_0^n$ and $\mathbf{V}_{N+1}^n$ are the values on two fake cells at two boundaries. Our iterative approach is listed below:

(1) Obtain the values $\mathbf{V}_0$ and $\mathbf{V}_{N+1}$ through the boundary conditions, Eq. (40), from initial values $\mathbf{V}_i$, $i = 1, 2, \ldots, N$.

(2) Guess the values of $\mathbf{V}_0^n$ and $\mathbf{V}_{N+1}^n$ as $\mathbf{V}_0$ and $\mathbf{V}_{N+1}$, respectively.

(3) Iteratively solve Eq. (39) for $\mathbf{V}_i^n$ ($i = 1, 2, \ldots, N$) to a required accuracy, but keep $\mathbf{V}_0^n$ and $\mathbf{V}_{N+1}^n$ fixed during the iteration.

(4) From Eq. (39), find Jacobi coefficients $\partial\mathbf{V}_1^n/\partial\mathbf{V}_0^n$, $\partial\mathbf{V}_1^n/\partial\mathbf{V}_{N+1}^n$, $\partial\mathbf{V}_N^n/\partial\mathbf{V}_0^n$, and $\partial\mathbf{V}_N^n/\partial\mathbf{V}_{N+1}^n$.

(5) From the boundary conditions, Eq. (40), and the values $\partial\mathbf{V}_1^n/\partial\mathbf{V}_0^n$ and $\partial\mathbf{V}_N^n/\partial\mathbf{V}_{N+1}^n$, find corrections, $\Delta\mathbf{V}_0^n$ and $\Delta\mathbf{V}_{N+1}^n$, of the initial guess.

(6) Modify the values of $\mathbf{V}_0^n$ and $\mathbf{V}_{N+1}^n$, $\mathbf{V}_0^n = \mathbf{V}_0^n + \Delta\mathbf{V}_0^n$, $\mathbf{V}_{N+1}^n = \mathbf{V}_{N+1}^n + \Delta\mathbf{V}_{N+1}^n$, and go back to the step (3).

We explain the steps listed above in more detail here. In step (2), we guess only eight values since $\mathbf{V}_0^n$ and $\mathbf{V}_{N+1}^n$ are vectors with four elements. In step (3) we iteratively solve Eq. (39) for $\mathbf{V}_i^n$ ($i = 1, 2, \ldots, N$) as described in the last subsection. It should be emphasized that during the iteration, the values of $\mathbf{V}_0^n$ and $\mathbf{V}_{N+1}^n$ are fixed. Therefore, in this step, we need only a few iterations if we use the sweeping method. After this step the solutions for $\mathbf{V}_i^n$ ($i = 0, 1, 2, \ldots, N$) do not necessarily satisfy the the boundary conditions, Eq. (40). If the boundary conditions are satisfied, then we get the solutions. Otherwise, we have to go to the next step. As a result of step (3), the values of $\mathbf{V}_1^n$ and $\mathbf{V}_N^n$ depend on $\mathbf{V}_0^n$ and $\mathbf{V}_{N+1}^n$. We may adjust the values of $\mathbf{V}_0^n$ and $\mathbf{V}_{N+1}^n$ so that Eq. (40) holds. Therefore, we may use the set of Eq. (40) to find a correction, $\Delta\mathbf{V}_0^n$ and $\Delta\mathbf{V}_{N+1}^n$, of the initial guess $\mathbf{V}_0^n$ and $\mathbf{V}_{N+1}^n$. The corrections are the solutions of the following set of eight equations

$$H_j\left(\mathbf{V}_0^n + \Delta\mathbf{V}_0^n, \mathbf{V}_{N+1}^n + \mathbf{V}_{N+1}^n,\ \mathbf{V}_1^n + \frac{\partial\mathbf{V}_1^n}{\partial\mathbf{V}_0^n}\Delta\mathbf{V}_0^n + \frac{\partial\mathbf{V}_1^n}{\partial\mathbf{V}_{N+1}^n}\Delta\mathbf{V}_{N+1}^n,\right.$$
$$\left.\mathbf{V}_N^n + \frac{\partial\mathbf{V}_N^n}{\partial\mathbf{V}_0^n}\Delta\mathbf{V}_0^n + \frac{\partial\mathbf{V}_N^n}{\partial\mathbf{V}_{N+1}^n}\Delta\mathbf{V}_{N+1}^n\right) = 0, \qquad j = 1, 2, \ldots, 8. \tag{41}$$

In Eq. (41), $\mathbf{V}_1^n$ and $\mathbf{V}_N^n$ are the solutions of step (3). The Jacobi coefficients, $\partial\mathbf{V}_1^n/\partial\mathbf{V}_0^n$, $\partial\mathbf{V}_1^n/\partial\mathbf{V}_{N+1}^n$, $\partial\mathbf{V}_N^n/\partial\mathbf{V}_0^n$, and $\partial\mathbf{V}_N^n/\partial\mathbf{V}_{N+1}^n$, represent the dependence of the solutions, $\mathbf{V}_1^n$ and $\mathbf{V}_N^n$, on the initial guess $\mathbf{V}_0^n$ and $\mathbf{V}_{N+1}^n$. The Jacobi coefficients may be obtained from Eq. (39). In order to find the Jacobi coefficients, we take the derivative of Eq. (39) with respect to v^n, which is any one of elements in $\mathbf{V}_0^n$ and $\mathbf{V}_{N+1}^n$. Thus we have

$$\hat{\mathbf{Q}}_i\hat{\mathbf{V}}_i^n = \hat{\mathbf{P}}_i\hat{\mathbf{V}}_{i+1}^n + \hat{\mathbf{M}}_i\hat{\mathbf{V}}_{i-1}^n. \tag{42}$$

Here

$$\hat{\mathbf{V}}_i^n \equiv \frac{\partial\mathbf{V}_i^n}{\partial v^n}.$$

Since $\mathbf{Q}_i$, $\mathbf{P}_i$, and $\mathbf{M}_i$ in Eq. (39) are not constant, the matrices $\hat{\mathbf{Q}}_i$, $\hat{\mathbf{P}}_i$, and $\hat{\mathbf{M}}_i$ depend on the unknowns $\hat{\mathbf{V}}_i^n$ as well as $\mathbf{V}_i^n$. Like Eq. (39), the system described by Eq. (42) is nonlinear too.

Exactly like Eq. (39), Eq. (42) may be iteratively solved. When we iteratively solve Eq. (42), the $\mathbf{V}_i^n$ are kept constant which are the solutions obtained in step (3). The boundary values, $\hat{\mathbf{V}}_0^n$ and $\hat{\mathbf{V}}_{N+1}^n$, in Eq. (42) are fixed. For example, if v^n is p_0^n, the boundary condition

used for Eq. (42) is

$$\hat{\mathbf{V}}_0^n = \begin{pmatrix} 1 \\ 0 \\ 0 \\ 0 \end{pmatrix}$$

and

$$\hat{\mathbf{V}}_{N+1}^n = 0.$$

Therefore, only a few of iterations are needed for Eq. (42) if the sweeping method is used. Since there are eight elements in $\mathbf{V}_0^n$ and $\mathbf{V}_{N+1}^n$, we have to solve Eq. (42) eight times, and each for one of the elements. After finding the Jacobi coefficients, we can find the corrections through solving Eq. (41).

The approach presented here is for general boundary conditions, Eq. (40). For typical boundary conditions used in applications, such as periodic boundary conditions, reflection boundary conditions, flow-in and flow-out boundary conditions, the forms of Eqs. (40), (41) are very simple. For example, for periodic boundary conditions, the form of Eq. (40) is

$$\mathbf{V}_1^n = \mathbf{V}_{N+1}^n,$$
$$\mathbf{V}_N^n = \mathbf{V}_0^n,$$

and the form of Eq. (41) is

$$\mathbf{V}_1^n + \sum_v \frac{\partial \mathbf{V}_1^n}{\partial v^n} \Delta v^n = \mathbf{V}_{N+1}^n + \Delta \mathbf{V}_{N+1}^n,$$
$$\mathbf{V}_N^n + \sum_v \frac{\partial \mathbf{V}_N^n}{\partial v^n} \Delta v^n = \mathbf{V}_0^n + \Delta \mathbf{V}_0^n.$$

Together with the sweeping method, we call the approach the accelerated approach. Applying this accelerated approach to the wave described before with $N\ (=256)$ grid cells and the time step $\Delta t = 7 \times 10^{-3}$, we obtain the convergence shown in Fig. 9. The horizontal coordinate in the figure is the number of iterations used for iteratively solving Eq. (39). As stated before, for each of eight Jacobi coefficients, we also iteratively solve Eq. (42). For each point on a curve shown in Fig. 9, Eq. (42) is solved only once for each element of $\mathbf{V}_0^n$ and $\mathbf{V}_{N+1}^n$, i.e., step (4) described above is implemented only once. For example, for the number of iterations 10, we use 5 iterations solving Eq. (39) before step (4), and we use another set of 5 iterations solving Eq. (39) after the values $\mathbf{V}_0^n$ and $\mathbf{V}_{N+1}^n$ are corrected once. In Fig. 10 we show the convergence vs the total number of iterations used for both Eq. (39) and Eq. (42) for all eight Jacobi coefficients.

The accelerated approach proposed above significantly reduces the cost of simulations. Compared to the approach shown in Fig. 7, for a given required accuracy, the accelerated approach shown in Fig. 10 reduces the number of iterations needed by more than one order. In our numerical examples to be shown, only less than 40 total iterations are needed in each time step, no matter how many cells radiation signals propagate in one time step. To measure the cost of each iteration, we run our code 1000 time steps, and in each time step, we allow 40 iterations. The total cost of this run is 36.1 s. We run the same code 1000 time

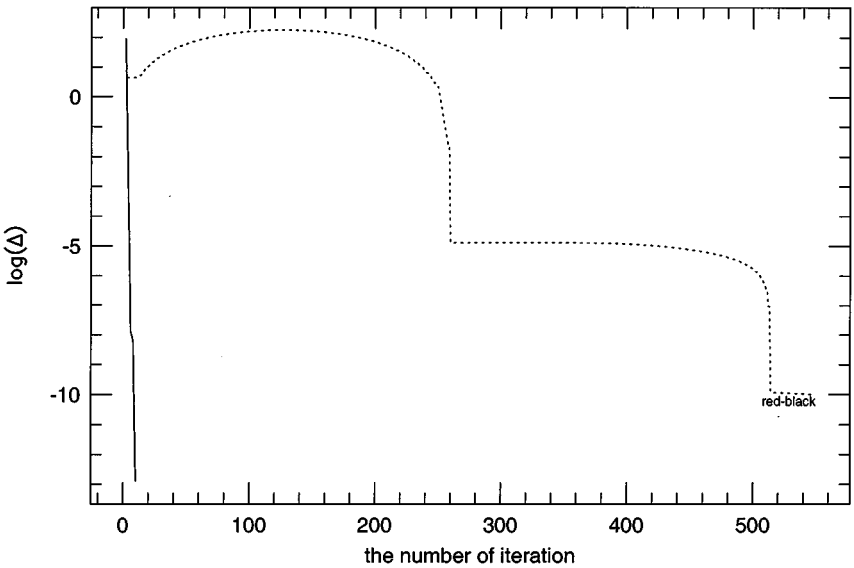

FIG. 9. The convergence obtained from the accelerated red–black (dashed line) and accelerated sweeping method (solid line) when $\Delta t c_r / \Delta x$ is about 17,920. The horizontal coordinate is the number of iterations used for Eq. (39).

steps again, but in each time step, we allow 50 iterations. The total cost of the second run is 38.3. From these numbers it is easy to find that each iteration costs 2.2×10^{-4} s and the each time step without any iteration costs 2.73×10^{-2} s. Therefore, each iteration costs only 0.8 percent of the CPU time which is used for a fully explicit scheme which is second order accurate both in space and time.

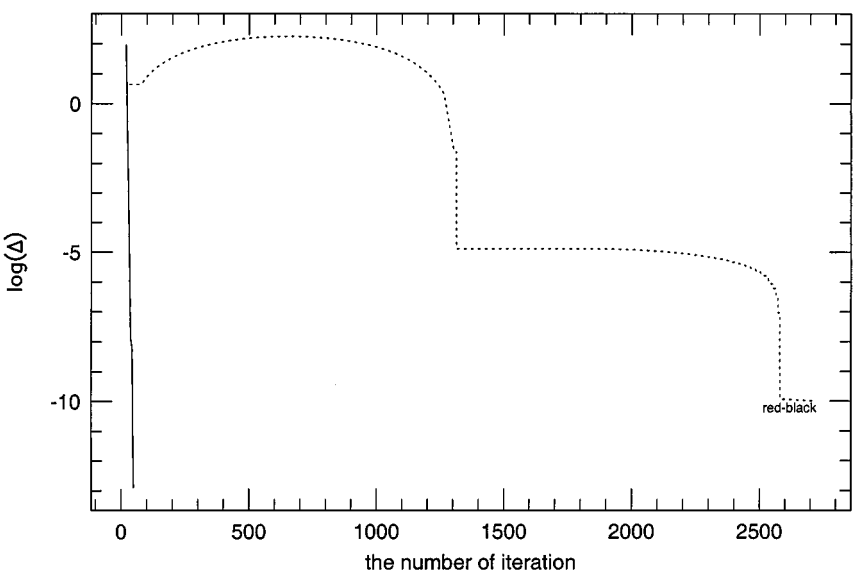

FIG. 10. The convergence obtained from the accelerated red–black (dashed line) and accelerated sweeping method (solid line) when $\Delta t c_r / \Delta x$ is about 17,920. The horizontal coordinate is the total number of iterations used for both Eq. (39) and Eq. (42) for all eight Jacobi coefficients.

4.5. *Consideration for Multi-dimensions*

The implicit treatment for radiation signals and the iterative approach described above may be directly applied to two-dimensional radiation hydrodynamical Eqs. (1)–(7). In this paper, we apply the dimensionally split technique originally proposed by Strang [3] for explicit schemes to our implicit–explicit hybrid calculation. The method for two-dimensional equations is the symmetric product of one-dimensional operators:

$$\mathbf{L}_{\Delta t} = \frac{1}{2}\left(\mathbf{L}^x_{\Delta t}\mathbf{L}^y_{\Delta t} + \mathbf{L}^y_{\Delta t}\mathbf{L}^x_{\Delta t}\right). \tag{43}$$

Here $\mathbf{L}^x_{\Delta t}$ is a one-dimensional operator with time step Δt for one-dimensional Eq. (8).

For a linear hyperbolic model problem,

$$\frac{\partial F}{\partial t} = A\frac{\partial F}{\partial x} + B\frac{\partial F}{\partial y},$$

where coefficients A and B are symmetric matrices and constant. Following the procedure provided in [3] it is easy to show that the operator $\mathbf{L}_{\Delta t}$ is second-order accurate if each one-dimensional operator is. For any smooth function $U(x, y, t)$, the second order accuracy requires that

$$\mathbf{L}_{\Delta t}U = U + \Delta t\left(A\frac{\partial U}{\partial x} + B\frac{\partial U}{\partial y}\right) + \frac{1}{2}\Delta t^2\left[A^2\frac{\partial^2 U}{\partial x^2} + (AB + BA)\frac{\partial^2 U}{\partial x\,\partial y} + B^2\frac{\partial^2 U}{\partial y^2}\right] + O(\Delta t^3). \tag{44}$$

Since each one-dimensional operator is second order accurate, i.e.,

$$\mathbf{L}^x_{\Delta t}U = U + \Delta t A\frac{\partial U}{\partial x} + \frac{1}{2}\Delta t^2 A^2\frac{\partial^2 U}{\partial x^2},$$

$$\mathbf{L}^y_{\Delta t}U = U + \Delta t B\frac{\partial U}{\partial y} + \frac{1}{2}\Delta t^2 B^2\frac{\partial^2 U}{\partial y^2}.$$

Applying the operator $\mathbf{L}_{\Delta t}$ defined in Eq. (43) on a smooth function $U(x, y, t)$, and using the two equations above, we may find that Eq. (44) is valid. Therefore, each time step for a two-dimensional problem is divided into four one-dimensional sweeps.

In this paper, we will use the approach Eq. (43) for two-dimensional radiation hydrodynamical Eqs. (1)–(7). The one-dimensional operator $\mathbf{L}^x_{\Delta t}$ is the solver described before for one-dimensional Eq. (8). The size of time step is limited by the maximum value of wave speeds $|u_x \pm c_s|$ and $|u_y \pm c_s|$ involved in all four one-dimensional operations in the whole simulation domain. The accelerated approach may be applied to the two-dimensional situation. The way we use in this paper is very straightforward. For example, the K iterations for a two-dimensional problem are achieved through K iterations carried out in each of four one-dimensional sweeps in Eq. (43).

5. NUMERICAL EXAMPLES

The numerical scheme described in this paper has been tested for some problems for the correctness and robustness, a few of which are presented here to illustrate the features of the

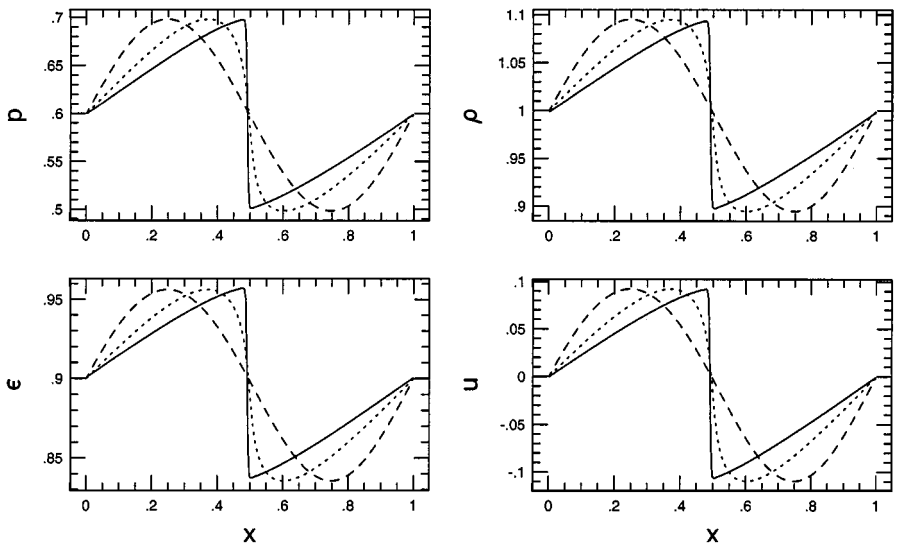

FIG. 11. The numerical solution for the case of the Euler equations. The dashed lines are initial conditions, dotted lines are the solution at $t = 1.0$ and the solid lines are the solution at $t = 2.0$.

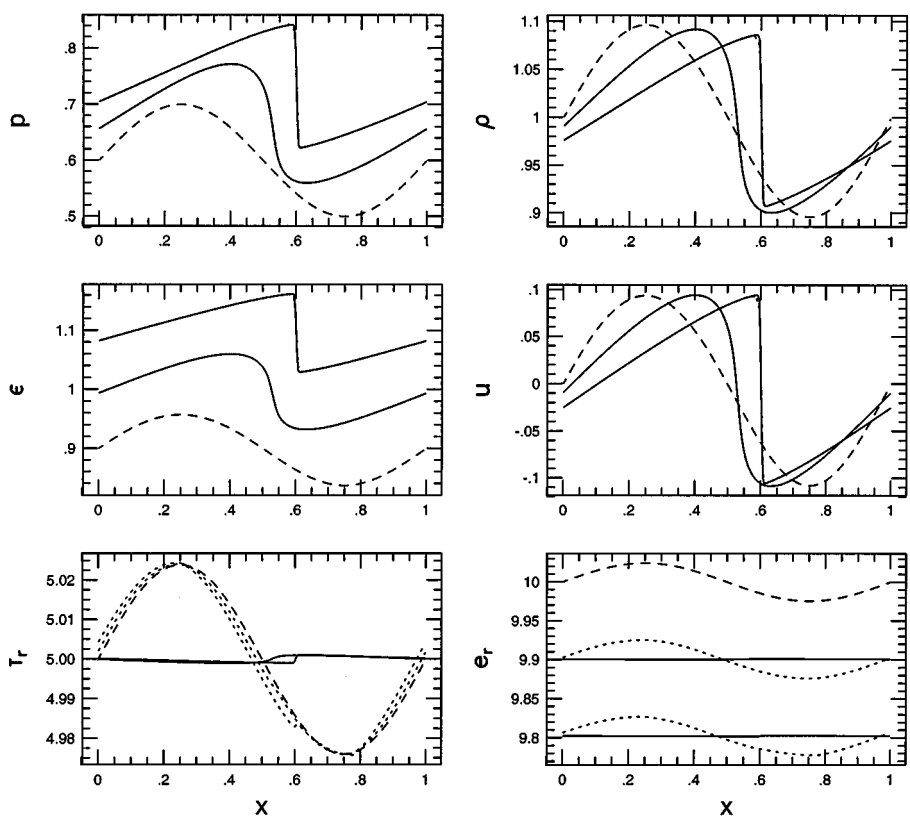

FIG. 12. The numerical solution for the case of radiation hydrodynamics with $c\kappa_e = 0.01$. The dashed lines are initial conditions, and the solid lines are the solution at $t = 1$ and $t = 2$. The dotted lines, which are hidden behind solid lines, are obtained from a fully explicit scheme.

scheme. In all the examples, γ and f_E are set to 5/3 and 1, respectively. Unless specified otherwise, the size of time step is such chosen that the Courant number for sound waves is about 0.8. In each numerical example, we use the accelerated approach, and a required accuracy used in step (3) in Subsection 4.4 is chosen to be 10^{-7}.

The first set of four simulations is for the propagation of smooth waves. Initially we set up a sound wave and a radiation wave through dR_{s+} and dR_{r+}. The sound wave speed is about unity, and c is set to 2000. In the first run, e_r, f_x, and radiation coefficients are all set to zero. The dashed lines in Fig. 11 are the initial profiles, and the dotted and solid lines in Fig. 11 show the profiles at $t = 1.0$ and $t = 2.0$, respectively. The smooth wave becomes a shock when propagating. In the second run, we set $c\kappa_e$ equal to 0.01 and the initial profiles are shown through the dashed lines in Fig. 12. The solid lines in Fig. 12 show the profiles at $t = 1.0$ and $t = 2.0$. It is interesting to compare the results with those obtained from a fully explicit and second order accurate scheme in which the size of time step is limited by the radiation speed. The dotted lines in Fig. 12, which are almost hidden behind solid lines for ρ, p, and u, are obtained from the fully explicit scheme. There are little differences in flow fields between the two sets of solution. The third run is for a flow with a finite emissivity κ_p. The initial profiles are shown through dashed lines in Fig. 13. $c\kappa_p a_r$ is set to 0.05. The solid lines in Fig. 13 show the profiles at $t = 1.0$ and $t = 2.0$. The internal energy of flow decreases while the radiation energy increases with time. In Fig. 13 we also give

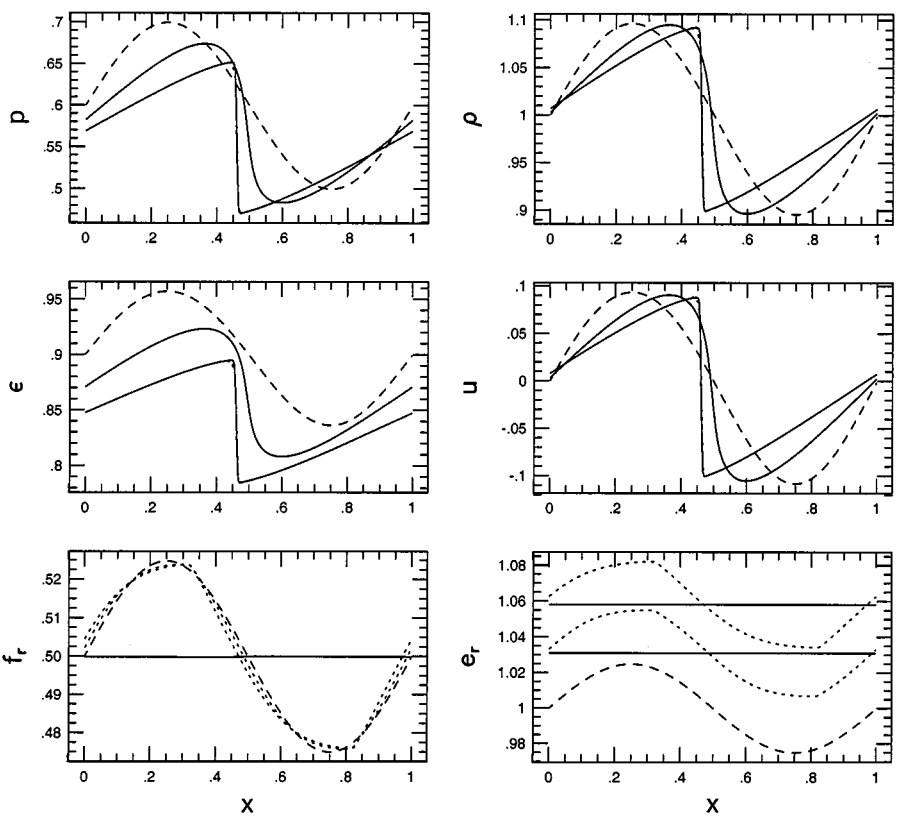

FIG. 13. The numerical solution for the case of radiation hydrodynamics with $ca_r\kappa_p = 0.05$. The dashed lines are initial conditions, and the solid lines are the solution at $t = 1$ and $t = 2$. The dotted lines, which are hidden behind solid lines, are obtained from a fully explicit scheme.

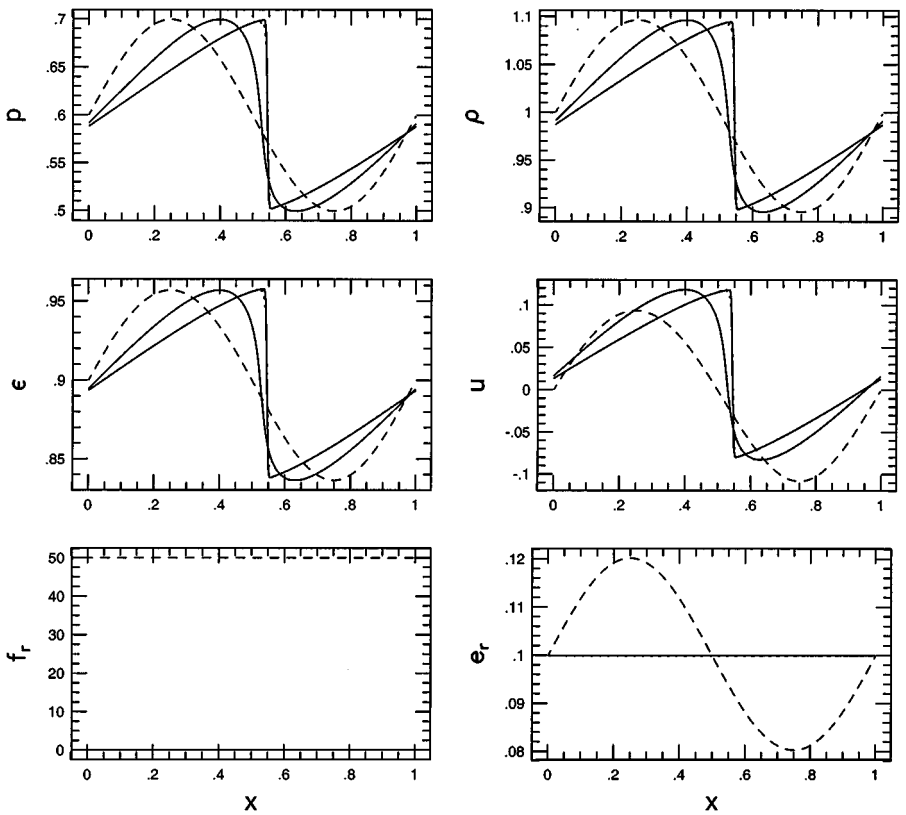

FIG. 14. The numerical solution for the case of radiation hydrodynamics $\chi = 0.2$. The dashed lines are initial conditions, and the solid lines are the solution at $t = 1$ and $t = 2$. The dotted lines, which are hidden behind solid lines, are obtained from a fully explicit scheme.

the numerical solution (dotted lines) obtained from the fully explicit scheme. It is hard to see differences in flow fields between the two sets of solution. The fourth run is to show the acceleration due to the radiation flux. The initial profiles are shown in Fig. 14 through the dashed lines. The momentum absorption coefficient χ is set to 0.2. The solid lines in Fig. 14 show the profiles at $t = 1.0$ and $t = 2.0$. The flow is accelerated through the radiation flux. In Fig. 14 we also give the numerical solution (dotted lines) obtained from the fully explicit scheme.

Next, we would like to demonstrate the accuracy of the scheme. Initially, we set up two waves through dR_{s+} and dR_{r+}, which are shown by the dashed lines in Fig. 15. The sound speed is about unity. The light speed c is set to 5000, and $c\kappa_p a_r$ is equal to 0.01. We run the problem using six grids with 256, 128, 64, 32, 16, and 8 grid points. The solid lines in Fig. 15 show six sets of solution at $t = 10$ obtained from these six grids. It is hard to see differences in the results for the three grids with 64, 128, and 256 grid points. To show the correctness of the solution, in Fig. 16 we plot the numerical solution (solid lines) with 256 grid points against a solution obtained from a fully explicit scheme (dotted lines completely hidden behind the solid lines).

The next set of examples involve Mach 3 shocks. We first test the case of the Euler equations. In Fig. 17, the dashed lines in the plots for ρ, p, u, and ϵ are the initial profiles, and the dotted lines are the numerical solution at $t = 0.15$ for the Euler equations. For

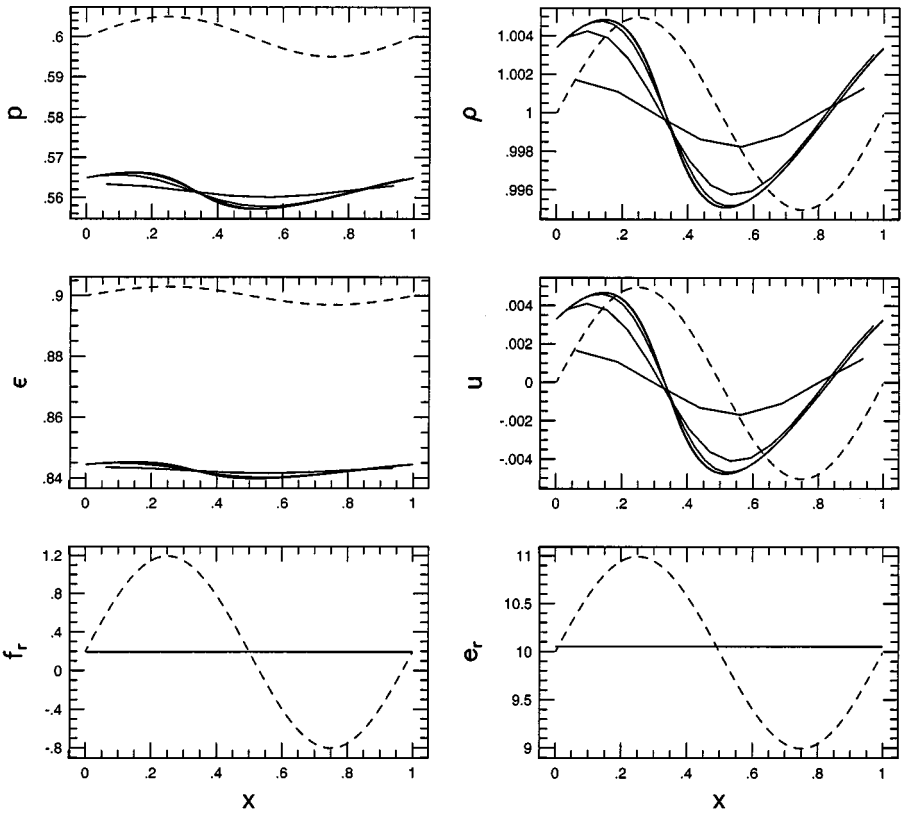

FIG. 15. The numerical solution after a sound wave propagates about ten wavelengths. The dashed lines are initial profiles, and the solid lines are the solution obtained from six simulations which have the different numbers of grid points. The six grids have 8, 16, 32, 64, 128, and 256 grid points. The three sets of solution obtained from three grids with 64, 128, and 256 grid points are almost identical.

radiation hydrodynamical equations, we add radiation energy and flux in this problem, as shown by the dashed lines in the plot for e_r and f_x. We set $c\kappa_p a_r$ equal to 0.05 and the light speed c equal to 5000. The numerical solution at $t = 0.15$ for radiation hydrodynamical equations is shown by the solid lines in Fig. 17. A direct effect of the finite κ_p in this problem is the increase of the radiation energy e_r and the decrease of the internal energy $\rho\epsilon$. The flow velocity and radiation flux are also changed. To compare the numerical solution with those obtained from the fully explicit scheme, in Fig. 18 we give the two sets of solution against each other. The dotted lines, which are completely hidden behind the solid lines, are the solution obtained from the fully explicit scheme.

The final one-dimensional example is a Mach 10 shock impacting on a denser region. The sound speed in the pre-shock state is unity. The gas in the denser region is 100 times denser than that in the pre-shock state. The dashed lines in Fig. 19 show the initial profiles. The solid lines in the figure are the solution of the Euler equations at $t = 0.05$. For radiation hydrodynamics, the light speed c is set to 10^5, and we let radiation fields get into the simulation domain through the left boundary, i.e., we set $(e_r,\ f_x)$ to (10, 0.1) at $x = 0$ as a boundary condition. $c\kappa_e$ is set to 25, and κ_p and χ are set to zero. The solid lines in Fig. 20 are the solution at $t = 0.05$.

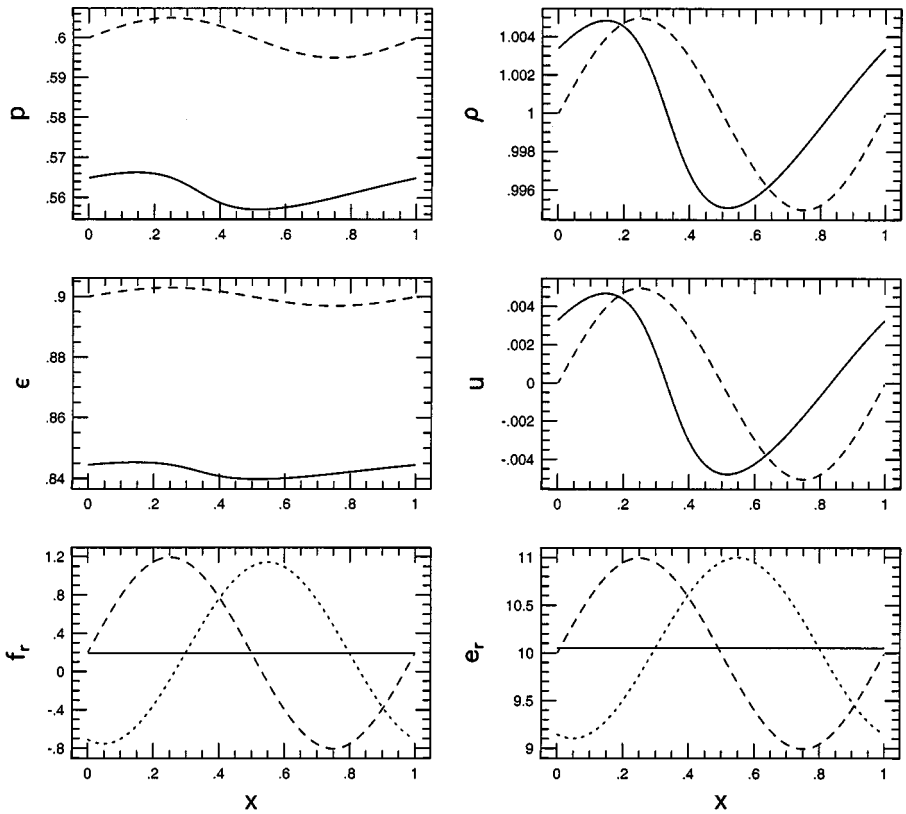

FIG. 16. The numerical solution after a sound wave propagates about ten wavelengths. Dashed lines are initial profiles, the solid lines are obtained from the implicit-explicit scheme, and the dotted lines, which are completely hidden behind the solid lines and can't be seen, are obtained from a fully explicit scheme.

The remaining examples are for the two-dimensional situation. The first two two-dimensional simulations are carried on a two-dimensional domain $(L_x - 0) \times (L_y - 0)$, where $L_x \equiv 1/\cos\alpha$, $L_y \equiv 1/\sin\alpha$, and $\alpha = 30^0$, periodic boundaries conditions are used in both x- and y-directions, and the simulations are about waves propagating at the direction which is at α degree with respect to the x-axis.

The first two-dimensional example is to show the convergence in the numerical solution for smooth flow. Initially, we set up a sound wave with about unity wave speed and a radiation wave with c equal 10^3 propagating at the α-direction. The dashed lines in Fig. 21 show the initial profiles along the line $y = L_y/2$. The solid lines in Fig. 21 show the numerical solution after the sound wave propagates ten wavelengths, which are obtained from five simulations through five grids with 8^2, 16^2, 32^2, 64^2, and 128^2 grid points. The differences between the two sets of solution of 64^2 and 128^2 are difficult to be noticed. To demonstrate the correctness of the converged solution of flow motion, in Fig. 22 we plot the numerical solution (solid lines) against the solution obtained from the fully explicit one-dimensional scheme (dotted lines). There are no differences in flow motion between two sets of solution, although they are obviously different in radiation fields.

The second example is about the steepening of a sound wave in a two-dimensional domain. Initially a sound wave and a radiation wave are set up propagating along the α-direction.

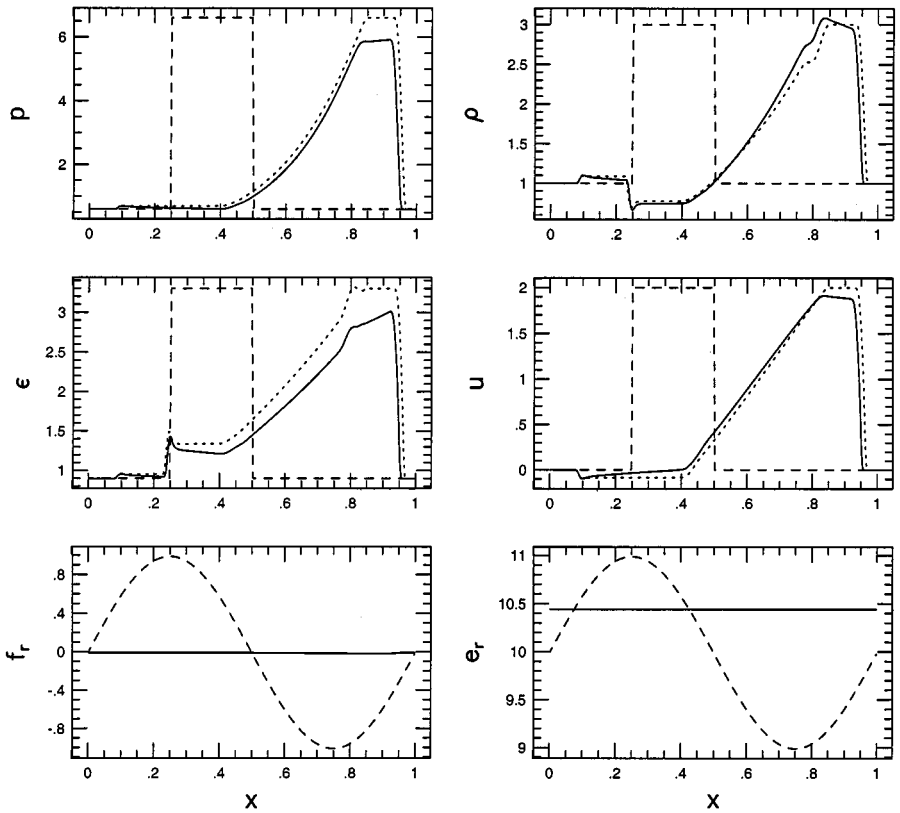

FIG. 17. The numerical solution for the propagation of a Mach 3 shock at $t = 0.15$. Dashed lines are initial profiles. The dotted lines are the results for the case of the Euler equations in which radiation quantities are all zero. The solid lines are the results for radiation hydrodynamical equations in which $ca_r\kappa_p = 0.01$.

The sound wave speed is about unity, $c = 2 \times 10^3$ and $ca_r\kappa_p = 0.02$. A grid with 128^2 points is used in the simulation domain. The dashed lines in Fig. 23 show the initial profiles along the line $y = L_y/2$, and the solid lines in Fig. 23 are the numerical solution after the sound wave propagates one and two wavelengths. For a comparison, in Fig. 23 we also give the solution (dotted lines) obtained from the fully explicit one-dimensional scheme, which are hidden behind the solid lines.

The next example is interaction between a Mach 10 shock and a denser cloud. A circular cloud is initially located in front of a Mach 10 shock, and the cloud is 10^3 times denser than the pre-shock state. The sound wave speed in the pre-shock state is unity and the light speed c is set to 10^5. The radiation coefficients χ and κ_p are set to zero, and $c\kappa_e$ is set to 2.5. The simulation is carried on a 20×10 domain. Initially radiation fields e_r, f_x, and f_y are zero in the simulation domain. As a boundary condition at the left side, we set constant values for $(\rho, p, u_x, e_r, f_x, f_y)$, (ρ, p, u_x) take the values at the post-shock state, and (e_r, f_x, f_y) take $(10, 10^4, 0)$. An open boundary condition is used at other three sides of the simulation domain. The simulation is carried out with a grid resolution 1024×512. The upper image in Fig. 24 displays the temperature at one instant. As a comparison, in the lower image of Fig. 24, we also give the solution of the Euler equations at the same instant. As shown in the figure, the flow is heated through absorbing radiation energy. We have to point out that

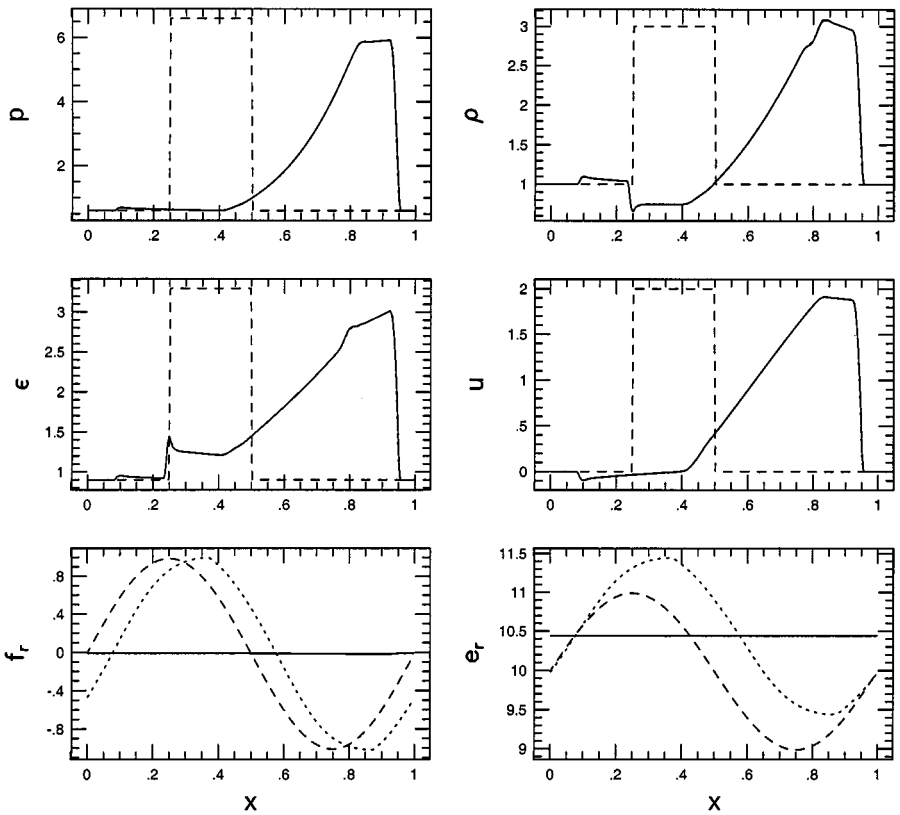

FIG. 18. The numerical solution (solid lines) at $t = 0.15$ are plotted against the solution obtained from a fully explicit scheme (dotted lines completely hidden behind the solid lines). Dashed lines are initial profiles.

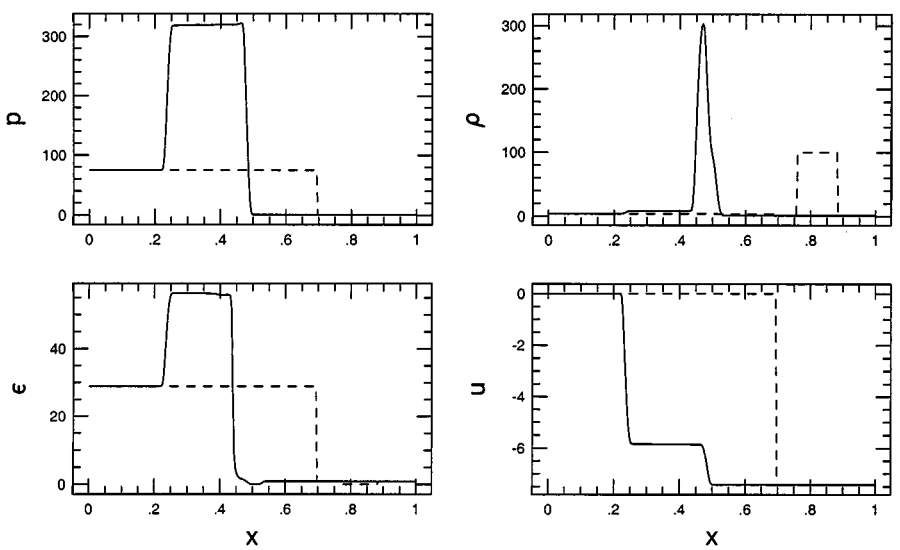

FIG. 19. The numerical solution for the case of the Euler equations for a Mach 10 shock interacting with a denser region. The dashed lines are initial profiles, and the solid lines are the solution at $t = 0.05$.

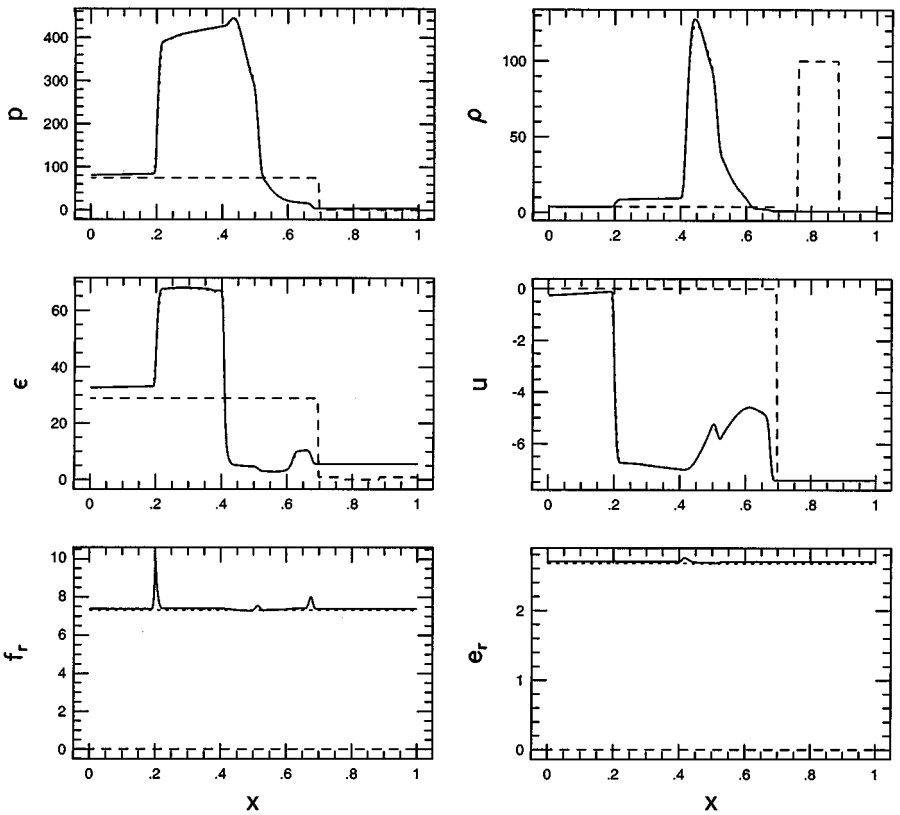

FIG. 20. The numerical solution for the case of radiation hydrodynamics with $c\kappa_e = 25$. Dashed lines are initial profiles, solid lines are the solution at $t = 0.05$, and dotted lines, which are completely hidden behind the solid lines, are obtained from a fully explicit scheme. Constant values (10, 0.1) are assigned to the radiation fields (e_r, f_x) at the left boundary as a boundary condition.

we actually simulated a half of the domain, and the other half is duplicated according to the symmetry of the problem.

6. CONCLUSIONS AND DISCUSSIONS

In this paper, we have proposed a numerical scheme for two-dimensional radiation hydrodynamical equations in the transport limit. The scheme is of Godunov-type, in which the set of time-averaged flux is calculated through Riemann problems solved. In the scheme, flow signals are explicitly treated, while radiation signals are implicitly treated. Flow fields and radiation fields are updated simultaneously in the scheme. Numerical errors for radiation signals undergo strong damping in the scale of flow motion. The set of nonlinear algebraic equations arising from the implicitness of the scheme is iteratively solved, and the treatment is completely nonlinear. The sweeping method used in the scheme significantly reduces the number of iterations or computer CPU time needed. The accelerated approach proposed in this paper further reduces the number of iterations needed by more than one order. No mater how many cells radiation signals propagate in one time step, only an extremely small number of iterations are needed. Each iteration costs only 0.8 percent of the CPU time which is spent for one time step of a second order accurate and fully explicit scheme. From

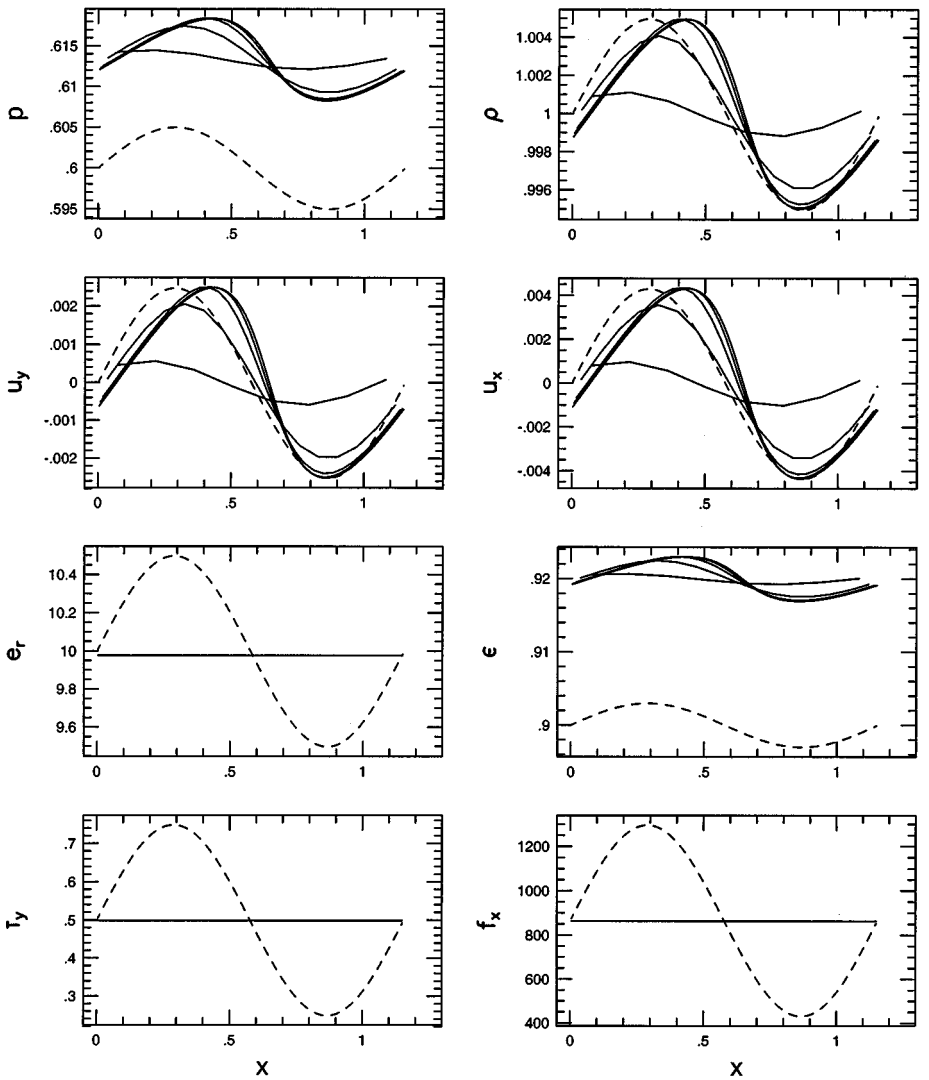

FIG. 21. Five sets of numerical solution for waves obliquely propagating in a two-dimensional domain, which are obtained through 8^2, 16^2, 32^2, 64^2, and 128^2 grid points. The dashed lines are initial conditions, and the solid lines are the solution after a sound wave propagates ten wavelengths. It is hard to see differences among the two sets of solution obtained through 64^2 and 128^2 grid points.

numerical examples, it is shown that the proposed scheme keeps the principle advantages of Godunov schemes for flow motion. In the time scale of flow motion, the numerical solution obtained from the implicit–explicit scheme is the same as that obtained from a fully explicit scheme which is second order accurate in both space and time.

The accelerated approach presented in this paper may be applied to other multi-coloring besides the red–black approach and may be applied to other hyperbolic systems of conservation laws, such as Euler equations and magnetohydrodynamical equations. We have applied the accelerated approach to the multi-coloring presented in [39], and the number of iterations needed in [39] is dramatically reduced.

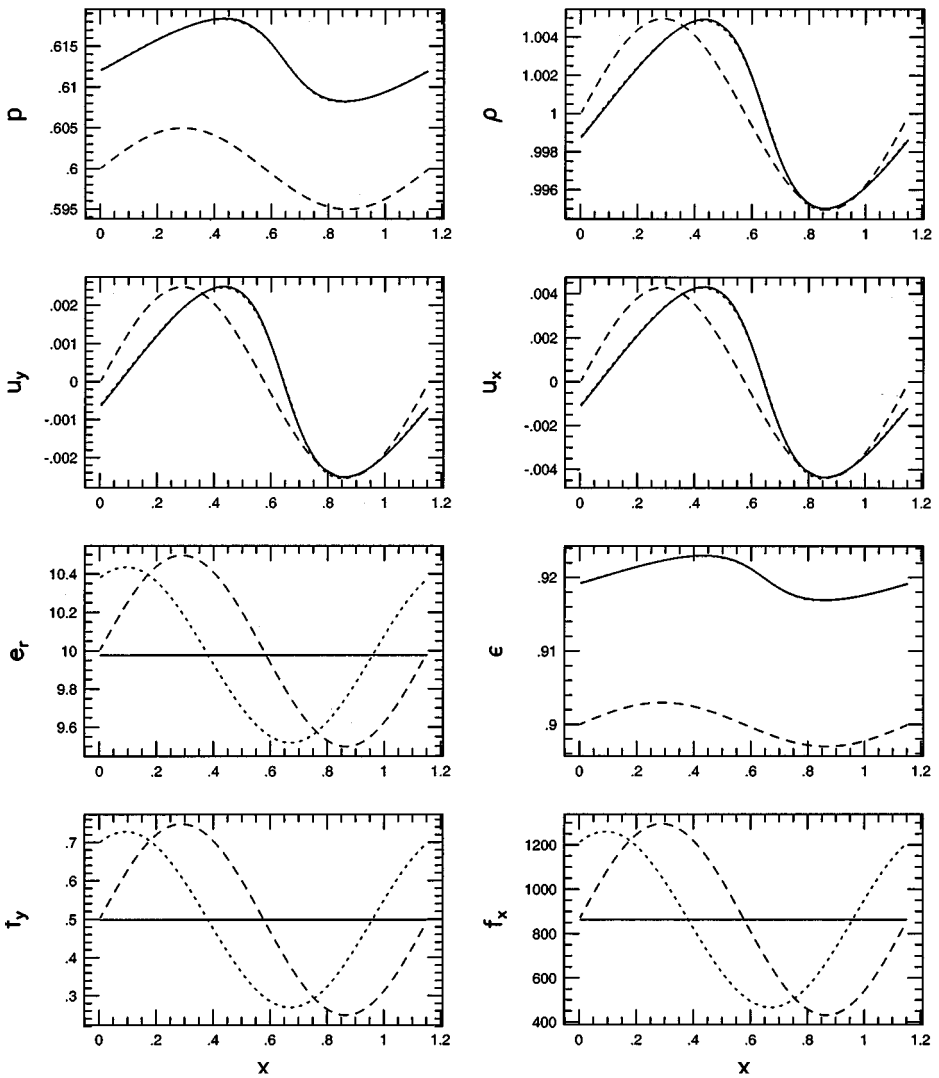

FIG. 22. A comparison in numerical solution between our two-dimensional implicit–explicit hybrid scheme (solid lines) and a fully explicit and one-dimensional scheme (dotted lines completely hidden behind the solid lines). The dashed lines are the initial profiles along the line $y = L_y/2$, and solid lines the solution after the sound wave propagates ten wavelengths.

The rate of convergence of the scheme will be influenced by the values of transport coefficients, since the source terms in Eqs. (1)–(7) are implicitly treated in the scheme. As an example, Fig. 25 shows the number of iterations needed vs the momentum absorption coefficient χ for a fixed tolerance. Here κ_p and κ_e are set to zero and the Courant number for radiation signals is 6.4×10^3.

In this paper, we have used a dimensionally split approach for two-dimensional problems. Compared to unsplit Godunov schemes, a dimensionally split approach is much cheaper in both CPU time and memory requirements. But it needs further investigation whether or not one can generally apply a split approach in implicit calculations although information may travel diagonally in a split approach. The split approach used in this paper is only the

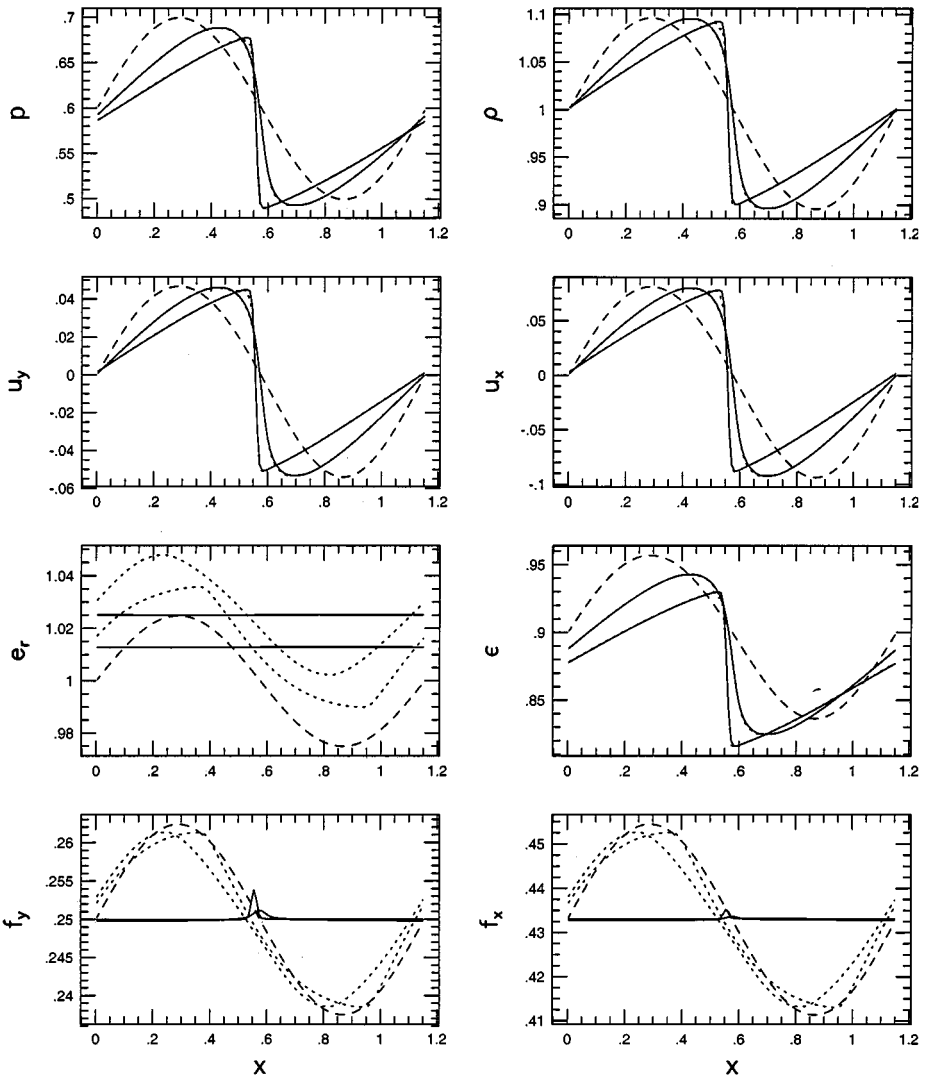

FIG. 23. A sound wave and a radiation wave obliquely propagate in a two-dimensional domain. Dashed lines are initial profiles along the line $y = Ly/2$, and two sets of solid lines are the solution after the sound wave propagates one and two wavelengths. The dotted lines hidden behind the solid lines are the solution obtained from a fully explicit one-dimensional scheme.

first step for multi-dimensional problems in radiation hydrodynamics. In this paper we have used the split approach Eq. (43). Compared to a typical split approach widely used for the Euler equations,

$$\mathbf{L}_{2\Delta t} = \mathbf{L}^x_{\Delta t}\mathbf{L}^y_{\Delta t}\mathbf{L}^y_{\Delta t}\mathbf{L}^x_{\Delta t}, \tag{45}$$

Eq. (43) doubled the cost. It is not clear whether Eq. (45), together with an iterative approach, may be used in implicit calculations for some problems.

The numerical scheme we proposed in this paper may be useful in numerical simulations for real problems, for which the equation of state and the constant Eddington factor for radiation fields should be changed. In real applications, specially in laser fusion, equations

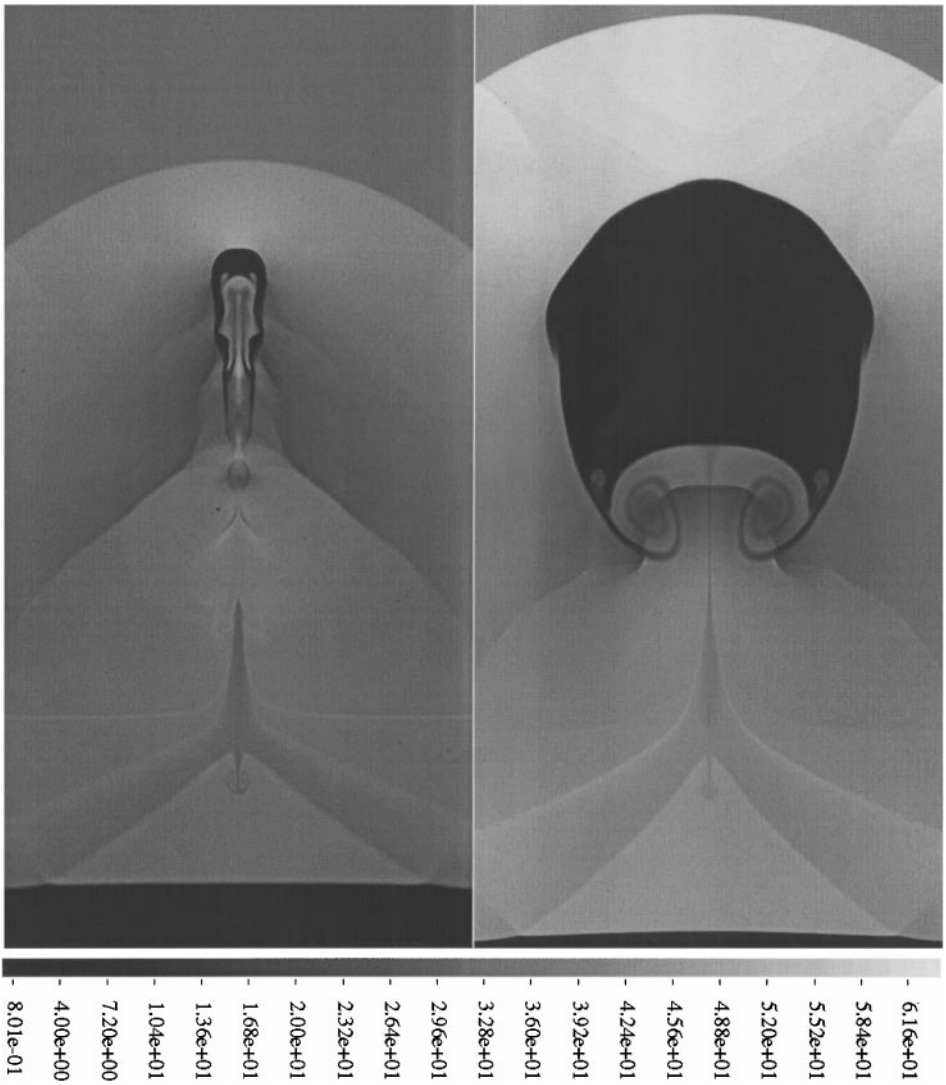

FIG. 24. The temperature in the interaction between a Mach 10 shock and a denser cloud. The cloud is 10^3 times denser than the pre-shock state. The radiation coefficients χ and κ_p are set to zero, and $c\kappa_e$ is set to 2.5. Initial radiation fields e_r, f_x, and f_y are zero. At the left boundary, the values of $(\rho, p, u_x, e_r, f_x, f_y)$ are fixed, ρ, p, and u_x take the values of the post-shock state, and e_r, f_x, and f_y take values 10, 10^4, and 0, respectively. An open boundary condition is used at the other three sides of the simulation domain. As a comparison, the lower image is the solution of the Euler equations at the same instant.

of state are much more complicated, and it may be tabular. The Eddington factor, if we can use, depends on radiation fields. The approach proposed in this paper, in principle, may be applied to this kind of equations of state, but each iteration of the iterative approach proposed in this paper will cost more since we have to numerically evaluate the equations of state in each iteration. Second, the distribution of photons in frequency has to be taken into consideration for real problems.

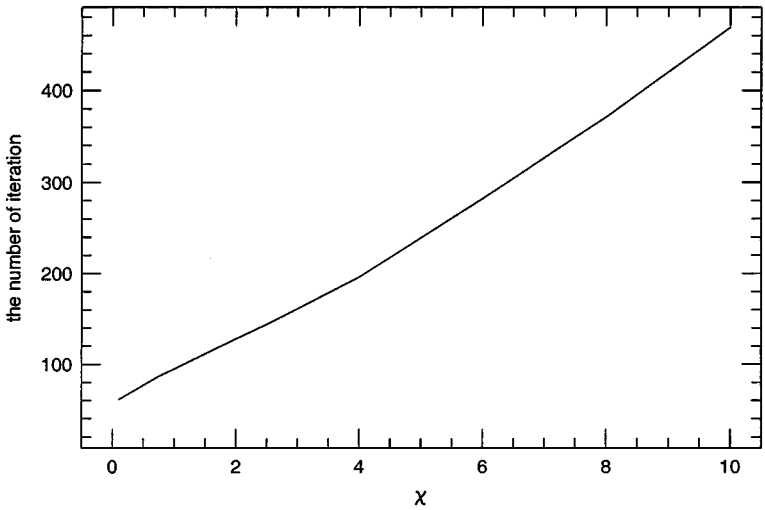

FIG. 25. The number of iteration needed vs the momentum absorption coefficient χ for fixed tolerance. κ_p and κ_e are set to zero and the Courant number for radiation signals is 6.4×10^3.

ACKNOWLEDGMENTS

The work presented here has been supported by the Department of Energy through Grants DE-FG02-87ER25035 and DE-FG02-94ER25207, by the National Science Foundation through Grant ASO-9309829, by NASA through Grant USRA/5555-23/NASA, and by the University of Minnesota through its Minnesota Supercomputer Institute.

REFERENCES

1. S. K. Godunov, Difference methods for the numerical calculation of the equations of fluid dynamics, *Math. Sb.* **47**, 271 (1959).
2. R. Courant and K. O. Friedrichs, *Supersonic Flow and Shock Wave*, 5th ed. (Interscience, New York, 1967).
3. G. Strang, On construction and comparison of differential schemes, *SIAM J. Numer. Anal.* **5**, 506 (1968).
4. J. Castor, Radiative transfer in spherically symmetric flows, *Astrophys. J.* **178**, 779 (1972).
5. R. W. Beam and R. F. Warming, An implicit finite-difference algorithm for hyperbolic systems in conservation-law form, *J. Comput. Phys.* **22**, 87 (1976).
6. B. van Leer, Toward the ultimate conservative difference scheme. V. A second-order sequel to Godunov's method, *J. Comput. Phys.* **32**, 101 (1979).
7. B. Engquist and S. Osher, Stable and entropy satisfying approximations for transonic flow calculations, *Math. Comput.* **34**, 45 (1980).
8. P. L. Roe, Approximate Riemann solvers, parameters vectors, and difference schemes, *J. Comput. Phys.* **43**, 357 (1981).
9. J. Glimm, E. Isaacson, D. Marchesin, and O. McBryan, Front tracking for hyperbolic system, *Adv. Appl. Math.* **2**, 91 (1981).
10. P. R. Woodward and P. Colella, High resolution difference schemes for compressible gas dynamics, in Lecture Notes in Phys. (Springer-Verlag, Berlin, 1981), Vol. 141, p. 434.
11. A. Harten, High resolution schemes for hyperbolic conservation laws, *J. Comput. Phys.* **49**, 357 (1983).
12. D. Mihalas and B. W. Mihalas, *Foundations of Radiation Hydrodynamics* (Oxford Univ. Press, New York, 1984).

13. P. R. Woodward and P. Colella, The numerical simulation of two-dimensional fluid flow with strong shocks, *J. Comput. Phys.* **54**, 115 (1984).
14. P. Colella and P. R. Woodward, The piecewise parabolic method (PPM) for gas-dynamical simulations, *J. Comput. Phys.* **54**, 174 (1984).
15. K.-H. A. Winkler, M. L. Norman, and D. Mihalas, Adaptive-mesh radiation hydrodynamics. I. The radiation transport equation in a completely adaptive coordinate system. *J. Quant. Spectrosc. Radiat. Transfer* **31**, 473 (1984).
16. D. Mihalas, K.-H. A. Winkler, and M. L. Norman, Adaptive-mesh radiation hydrodynamics. II. The radiation and fluid equations in relativistic flows. *J. Quant. Spectrosc. Radiat. Transfer* **31**, 479 (1984).
17. B. Van Leer and W. A. Mulder, in *Numerical Methods for the Euler Equations of Fluid Dynamics*, edited by F. Angrand, A. Dervieux, J. A. Desideri, and R. Glowinski (SIAM, Philadelphia, 1985), p. 312.
18. H. C. Yee, R. F. Warming, and A. Harten, Implicit total variation diminishing (TVD) schemes for steady-state calculations, *J. Comput. Phys.* **57**, 327 (1985).
19. H. M. Glaz and A. B. Wardlaw, A high-order Godunov scheme for steady supersonic gas dynamics, *J. Comput. Phys.* **58**, 157 (1985).
20. P. R. Woodward, Piecewise-parabolic methods for astrophysical fluid dynamics, in *Astrophysical Radiation Hydrodynamics*, edited by K.-H. A. Winkler and M. L. Norman (Reidel, Dordrecht, 1986), p. 245.
21. K.-H. A. Winkler and Michael L. Norman, Wh80s: Numerical radiation hydrodynamics, in *Astrophysical Radiation Hydrodynamics*, edited by K.-H. A. Winkler and M. L. Norman (Reidel, Dordrecht, 1986), p. 71.
22. B. A. Fryxell, P. R. Woodward, P. Colella, and K.-H. A. Winkler, An implicit-explicit hybrid method for Lagrangian hydrodynamics, *J. Comput. Phys.* **63**, 283 (1986).
23. A. Jameson and S. Yoon, Multigrid solution of the Euler equations using implicit schemes, *AIAA J.* **24**, 1737 (1986).
24. A. Jameson and S. Yoon, Lower-upper implicit schemes with multiple grids for the Euler equations, *AIAA J.* **25**, 929 (1987).
25. A. Harten and S. Osher, Uniformly high order accurate non-oscillatory schemes, I, *SIAM J. Numer. Anal.* **24**, 279 (1987).
26. A. Harten, B. Enquist, S. Osher, and S. R. Chakravarthy, Uniformly high order accurate essentially non-oscillatory schemes, III, *J. Comput. Phys.* **71**, 231 (1987).
27. J. B. Bell, P. Colella, and J. A. Trangenstein, Higher order Godunov methods for general systems of hyperbolic conservation laws, *J. Comput. Phys.* **82**, 362 (1989).
28. C. Y. Loh and W. H. Hui, A new Lagrangian method for steady supersonic flow computation. I. Godunov scheme, *J. Comput. Phys.* **89**, 207 (1990).
29. R. J. LeVeque, *Numerical Methods for Conservation Laws* (Birkhäuser, Basel, 1992).
30. M. Blunt and B. Rubin, Implicit flux-limiting schemes for petroleum reservoir simulation, *J. Comput. Phys.* **102**, 194 (1992).
31. M. Wilcoxson and V. Manousiouthakis, On an implicit ENO scheme, *J. Comput. Phys.* **115**, 376 (1994).
32. M. Gehmeyr and D. Mihalas, Adaptive grid radiation hydrodynamics with TITAN, *Phys. D* **77**, 320 (1994).
33. J. Lindl, Development of the indirect-drive approach to inertial confinement fusion and the target physics basis for ignition and Gain, *Phys. Plasmas* **2**, 2933 (1995).
34. J. P. Collins, P. Colella, and H. M. Glaz, An implicit-explicit Eulerian Godunov scheme for compressible flow, *J. Comput. Phys.* **116**, 195 (1995).
35. W. Dai and P. R. Woodward, A simple Riemann solver and high-order Godunov schemes for hyperbolic systems of conservation laws, *J. Comput. Phys.* **121**, 51 (1995).
36. A. P. Boss and E. A. Myhill, Second-order accurate radiative hydrodynamics and multidimensional protostellar collapse, *Compt. Phys. Comm.* **89**, 59 (1995).
37. E. A. Dorfi and M. U. Feuchtinger, Adaptive radiation hydrodynamics of pulsating stars, *Compt. Phys. Comm.* **89**, 69 (1995).
38. W. Dai and P. R. Woodward, Iterative implementation of an implicit-explicit hybrid scheme for hydrodynamics, *J. Comput. Phys.* **124**, 217 (1996).

39. W. Dai and P. R. Woodward, A second-order iterative implicit-explicit hybrid scheme for hyperbolic systems of conservation laws, *J. Comput. Phys.* **128**, 181 (1996).
40. W. Dai and P. R. Woodward, Numerical simulations for radiation hydrodynamics. I. Diffusion limit, *J. Comput. Phys.* **142**, 182 (1998).
41. C. Baldwin, P. N. Brown, R. Falgout, J. Jones, and F. Graziani, Iteractive linear solvers in a 2D radiation-hydrodynamics code: Methods and performance, *J. Comput. Phys.*, in press.
42. R. B. Lowrie and J. E. Morel, The coupling of radiation and hydrodynamics, *Astrophys. J.* **521**, 432 (1999).